

## RESEARCH ARTICLE

# Glial ER and GAP junction mediated $\text{Ca}^{2+}$ waves are crucial to maintain normal brain excitability

Shirley Weiss<sup>1,2</sup>  | Lauren C. Clamon<sup>1,3</sup> | Julia E. Manoim<sup>2</sup> | Kiel G. Ormerod<sup>1</sup> | Moshe Parnas<sup>2,4</sup> | J. Troy Littleton<sup>1,3,5</sup>

<sup>1</sup>The Picower Institute for Learning and Memory, Massachusetts Institute of Technology, Cambridge, Massachusetts, USA

<sup>2</sup>Department of Physiology and Pharmacology, Sackler School of Medicine, Tel Aviv University, Tel Aviv, Israel

<sup>3</sup>Department of Biology, Massachusetts Institute of Technology, Cambridge, Massachusetts, USA

<sup>4</sup>Sagol School of Neuroscience, Tel Aviv University, Tel Aviv, Israel

<sup>5</sup>Department of Brain and Cognitive Sciences, Massachusetts Institute of Technology, Cambridge, Massachusetts, USA

**Correspondence**

Shirley Weiss, Department of Physiology and Pharmacology, Sackler School of Medicine, Tel Aviv University, Tel Aviv 69978, Israel.  
Email: shirleyws@tauex.tau.ac.il

**Funding information**

German Research Foundation, Grant/Award Number: 408264519; Israel Science Foundation, Grant/Award Number: 343/18; Israeli Ministry of Science and Technology; NIH, Grant/Award Numbers: MH104536, NS40296

**Abstract**

Astrocytes play key roles in regulating multiple aspects of neuronal function from invertebrates to humans and display  $\text{Ca}^{2+}$  fluctuations that are heterogeneously distributed throughout different cellular microdomains. Changes in  $\text{Ca}^{2+}$  dynamics represent a key mechanism for how astrocytes modulate neuronal activity. An unresolved issue is the origin and contribution of specific glial  $\text{Ca}^{2+}$  signaling components at distinct astrocytic domains to neuronal physiology and brain function. The *Drosophila* model system offers a simple nervous system that is highly amenable to cell-specific genetic manipulations to characterize the role of glial  $\text{Ca}^{2+}$  signaling. Here we identify a role for ER store-operated  $\text{Ca}^{2+}$  entry (SOCE) pathway in perineurial glia (PG), a glial population that contributes to the *Drosophila* blood-brain barrier. We show that PG cells display diverse  $\text{Ca}^{2+}$  activity that varies based on their locale within the brain.  $\text{Ca}^{2+}$  signaling in PG cells does not require extracellular  $\text{Ca}^{2+}$  and is blocked by inhibition of SOCE, Ryanodine receptors, or gap junctions. Disruption of these components triggers stimuli-induced seizure-like episodes. These findings indicate that  $\text{Ca}^{2+}$  release from internal stores and its propagation between neighboring glial cells via gap junctions are essential for maintaining normal nervous system function.

**KEYWORDS**

$\text{Ca}^{2+}$  waves, *Drosophila*, perineurial glia, seizures, store-operated  $\text{Ca}^{2+}$  entry

## 1 | INTRODUCTION

Glial cells regulate multiple aspects of brain function, including synapse formation, neuronal excitability, synaptic transmission and blood flow dynamics (Barres, 2008). Astrocytes, a prominent class of central nervous system (CNS) glia, modulate neuronal properties through the secretion of neuroactive agents (gliotransmission), neurotransmitter buffering and ion homeostasis, in addition to their role in synaptogenesis and blood-brain barrier function (Khakh & Deneen, 2019; Nagai et al., 2021). Astrocytes display  $\text{Ca}^{2+}$  fluctuations heterogeneously distributed throughout different cellular microdomains

including cell bodies, processes and endfeet that directly contact synapses and blood vessels. Although the roles of glial  $\text{Ca}^{2+}$  dynamics are still being elucidated, they are hypothesized to allow astrocytes to respond to information from neighboring CNS cells and exert local modulatory control over various aspects of brain activity (Bindocci et al., 2017; Haustein et al., 2014; Jiang, Diaz-Castro, Looger, & Khakh, 2016; Khakh & Deneen, 2019; Otsu et al., 2015; Shigetomi et al., 2013; Stobart et al., 2018).

Multiple studies indicate mammalian astrocytes display complex and diverse  $\text{Ca}^{2+}$  signals. This glial  $\text{Ca}^{2+}$  activity can be spontaneous (Shigetomi, et al., 2013; Shigetomi, Tong, Kwan, Corey, & Khakh, 2012) or evoked by neuronal activity (Di Castro et al., 2011; Panatier et al., 2011), ranging from small microdomain events

Moshe Parnas and J. Troy Littleton are co-last authors.



(Haustein, et al., 2014; Shigetomi, et al., 2013; Shigetomi, Kracun, Sofroniew, & Khakh, 2010) to global  $\text{Ca}^{2+}$  waves that encompass entire astrocytic cells (Haustein, et al., 2014). Furthermore, differences in  $\text{Ca}^{2+}$  activity of astrocytes from different brain regions provide evidence for functional heterogeneity (Clarke, Taha, Tyzack, & Patani, 2021). These diverse macroscopic  $\text{Ca}^{2+}$  events in different astrocytes or astrocytic processes may arise from diverse microscopic signaling cascades that are functionally segregated and molecularly distinct within the cell (Bindocci, et al., 2017; Shigetomi, Bowser, Sofroniew, & Khakh, 2008).  $\text{Ca}^{2+}$  sources in astrocytes include  $\text{Ca}^{2+}$  entry via plasma membrane  $\text{Ca}^{2+}$  channels (Dunn, Hill-Eubanks, Liedtke, & Nelson, 2013), release from endoplasmic reticulum (ER) intracellular  $\text{Ca}^{2+}$  stores (Haustein, et al., 2014; Straub, Bonev, Wilkerson, & Nelson, 2006) and release from mitochondria (Agarwal et al., 2017). However, signaling pathways mediating  $\text{Ca}^{2+}$  fluctuations in different cellular compartments are not well defined. An understanding of the subcellular distribution of signaling mechanisms is critical for dissecting how glial activity modulates brain development and function.

The *Drosophila* model offers a simple nervous system that is highly amenable to cell-specific genetic manipulations to address the role of different  $\text{Ca}^{2+}$  signaling pathways in glial function. Several *Drosophila* glial subtypes influence neuronal function via distinct mechanisms downstream of their  $\text{Ca}^{2+}$  dynamics. For example, astrocytic  $\text{Ca}^{2+}$  regulates neurotransmitter uptake (Y. V. Zhang, Ormerod, & Littleton, 2017) and secretion of neuromodulators (Ma, Stork, Bergles, & Freeman, 2016), while disruption of  $\text{Ca}^{2+}$  signaling in *Drosophila* cortex glia impairs  $\text{K}^+$  buffering capacity (Weiss, Melom, Ormerod, Zhang, & Littleton, 2019). Synchronized  $\text{Ca}^{2+}$  waves in *Drosophila* subperineurial glia cells control nutrient-dependent reactivation of neural stem cells and subsequent brain growth (Holcroft et al., 2013; Speder & Brand, 2014).

The *Drosophila* CNS is separated from the surrounding hemolymph, the insect “blood”, by a barrier that is structurally and functionally similar to the mammalian Blood-Brain Barrier (BBB, Figure 1 (a), [DeSalvo et al., 2014; DeSalvo, Mayer, Mayer, & Bainton, 2011; Stork et al., 2008]). The *Drosophila* BBB covers the entire CNS with a flattened cell sheet consisting of two classes of glia, an outer layer of perineurial glia (PG) and an inner layer of subperineurial glia (SPG) (Yildirim, Petri, Kottmeier, & Klambt, 2019). Here, using a genetic screen for glial pathways that increase seizure susceptibility in *Drosophila*, we found that knockdown of dStim (the *Drosophila* homolog of the mammalian Stromal Interaction Molecule 1, Stim1, acting in the Store-Operated Calcium Entry pathway, SOCE) in PG cells leads to severe heat-shock (HS) induced seizures. By performing detailed  $\text{Ca}^{2+}$  imaging studies, we show that PG cells exhibit robust, complex and dynamic  $\text{Ca}^{2+}$  activity that significantly differs between PG cells that occupy different brain regions. In addition, we find these  $\text{Ca}^{2+}$  dynamics are independent of extracellular  $\text{Ca}^{2+}$ , originate from internal ER stores and spread as waves through gap junctions. Similar to dStim knockdown in PG cells, knockdown of Orai, a plasma membrane  $\text{Ca}^{2+}$  channel that is gated by dStim leading to  $\text{Ca}^{2+}$  influx and restoration of the ER  $\text{Ca}^{2+}$  store, or of Ryanodine receptor (RyR) that releases  $\text{Ca}^{2+}$  from the ER, also disrupt PG  $\text{Ca}^{2+}$  dynamics and increase seizure

susceptibility. Inhibiting the propagation of  $\text{Ca}^{2+}$  activity within the PG sheet through gap junctions recapitulates the behavioral phenotype of SOCE knockdown. Together, our data indicate that PG  $\text{Ca}^{2+}$  release from internal stores is essential to maintain normal nervous system function.

## 2 | METHODS

### 2.1 | *Drosophila* genetics and molecular biology

Flies were cultured on a standard medium at 22°C unless otherwise noted. All *Drosophila* lines used in this study are listed in Table 1. The UAS/Gal4 and LexAop/LexA systems were used to drive transgenes in glia using the indicated drivers. The UAS-*dsRNAi* flies used in the study were obtained from the VDRC (Vienna, Austria) or the TRiP collection (Bloomington *Drosophila* Stock Center, Indiana University, Bloomington, IN). UAS-*myr::GCaMP6s* was constructed by replacing GCaMP5 in the previously described *myr::GCaMP5* transgenic construct (Melom & Littleton, 2013). To generate UAS- and *lexAop-ER::GCaMP6f* flies, OER:GCaMP6f (gift from Mikoshiba Hiroko, [Niwa et al., 2016]) was subcloned into either pBID-UASc or pBID-LexAop plasmids using standard methods (Epoch Life Science Inc.). Transgenic flies were obtained by standard germline injection (BestGene Inc). For all experiments described, both male and female larvae or adults were used. For survival assays, embryos were collected in groups of ~50 and transferred to fresh vials ( $n = 3$ ). 3<sup>rd</sup> instar larvae, pupae or adult flies were counted. Survival rate (SR) was calculated as:

$$SR = \frac{N^{\text{live animals}}}{N^{\text{embryos}}}$$

For conditional expression using Tub-Gal80<sup>ts</sup>, animals of the designated genotype were reared at 22°C with Gal80 suppressing Gal4-driven transgene expression (*dStim<sup>RNAi</sup>*, *Orai<sup>RNAi</sup>* and *inx2<sup>DN</sup>*). Adult flies were then transferred to a 31°C incubator to inactivate Gal80 and allow Gal4 knockdown for the indicated period. For UAS/Gal4 inhibition by low temperature, PG > *Orai<sup>RNAi</sup>* animals were reared at 18°C to suppress Gal4-driven transgene expression. Adult flies were transferred to a 25°C incubator upon eclosion to allow Gal4 knockdown/overexpression for 1 day before testing for HS-induced seizures. For inhibiting transgene expression specifically in neurons, *Elav-Gal80* (Yang et al., 2009) was used.

### 2.2 | Behavioral analysis

For assaying temperature-sensitive seizures, adult males aged 1–2 days were transferred in groups of ~10–20 flies ( $n \geq 3$ , total # of flies tested in all assays was always >40) into preheated vials in a water bath held at the indicated temperature with a precision of 0.1°C. Seizures were defined as the condition in which the animal lies incapacitated on its back or side with legs and wings contracting

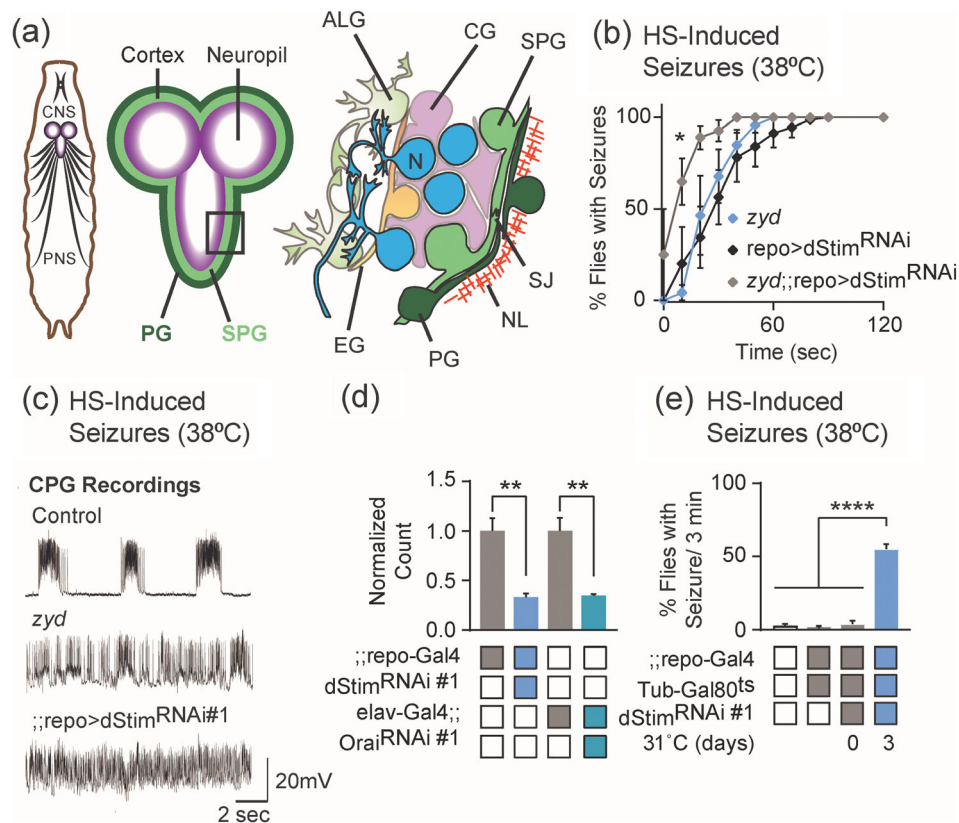


**FIGURE 1** Glial knockdown of *dStim* increases seizure susceptibility. (a) Schematic representation of the larval nervous system, showing five glial subtypes that occupy the CNS: perineurial glia (PG) and subperineurial glia (SPG) that form the blood–brain barrier (BBB), cortex glia (CG), and astrocyte-like glia (ALG) that directly contact neurons, and ensheathing glia (EG) that separate the cortex and neuropile. Neurons (N), septate junctions (SJ) and the neural lamina (NL) are also shown. (b) Time course of heat-shock induced seizures (38.5°C, HS) for *repo > dStim<sup>RNAi</sup>* is similar to that induced by the *zyd* mutation and enhanced in *repo > dStim<sup>RNAi</sup>* on the *zyd* mutation background, suggesting the two manipulations disrupt independent pathways to enhance seizure susceptibility ( $p < 0.05$ , Two-way ANOVA,  $N = 4$  groups of 20 flies/genotype, error bars are mean  $\pm$  SEM, see Video S1). (c) Representative voltage traces of spontaneous CPG activity recorded at larval 3<sup>rd</sup> instar muscle 6 at 38°C in wildtype, *zyd* and *repo > dStim<sup>RNAi</sup>* animals ( $n \geq 5$  preparations/genotype), showing *zyd* and *repo > dStim<sup>RNAi</sup>* animals lose normal rhythmic muscle activity at 38°C. (d) qRT-PCR analysis of *dStim* and *Orai* expression levels. The housekeeping gene *RPS3* (Ribosomal Protein S3) was used for normalization. Pan-glial *dStim* knockdown flies and pan-neuronal *Orai* knockdown flies have  $\sim 35\%$  of the control levels of *dStim* and *Orai* mRNAs, respectively. For complete data set, see Table S1. (e) Histogram summarizing the percent of flies exhibiting heat-shock induced seizures at 3 min (38.5°C) following conditional pan-glial knockdown of *dStim*. Rearing adult flies at the restrictive temperature ( $>30^\circ\text{C}$ ) with *Gal80<sup>ts</sup>* allows expression of *dStim<sup>RNAi</sup>* only at the adult stage. These manipulations partially reproduce the *repo > dStim<sup>RNAi</sup>* seizure phenotype ( $p < 0.0001$ , Student's *t* test,  $N = 4$  groups of 20 flies/genotype). \* =  $p < 0.05$ , \*\* =  $p < 0.01$ , \*\*\*\* =  $p < 0.0001$ .

vigorously (Melom & Littleton, 2013). For screening purposes, only flies that showed normal wild-type-like behavior (i.e. walking up and down on vial walls) after  $>2$  min of heat-shock were counted as not seizing. For assaying seizures in larvae, 3<sup>rd</sup> instar larvae were gently washed with PBS and transferred to 1% agarose plates or empty fly vials and heated to 38°C. Larval seizures were defined as continuous unpatterned contraction of the body wall muscles that prevented normal crawling behavior (Melom & Littleton, 2013). For determining seizure temperature threshold, groups of 10 animals were heat-shocked to the indicated temperature (ranging 30–39.0°C in 0.5°C increments). The threshold was defined as the temperature in which  $>50\%$  of the animals were seizing after 1 min.

For assaying bang sensitivity, adult male flies in groups of  $\sim 10$ –20 ( $n = 3$ ) were assayed 1–2 days post-eclosion. Flies were transferred into empty vials and allowed to rest for 1–2 h. Vials were

vortexed at maximum speed for 10 s and the number of flies that were upright and mobile was counted at 10 s intervals.

For larval activity monitoring, wandering 3<sup>rd</sup> instar larval activity was assayed using a multi-beam system (MB5, TriKinetics) as previously described (Green et al., 2015). Briefly, individual animals were inserted into  $5 \times 80$  mm glass pyrex tubes. The activity was recorded following a 5 min acclimation period. Throughout each experiment, animals were housed in a temperature- and light-controlled incubator (25°C,  $\sim 40\%$ –60% humidity). Post-acquisition activity analysis was performed using Excel to calculate activity level across 1-min time bins. Each experimental run contained eight control animals and eight experimental animals with  $n \geq 3$ .

For adult speed assays, 5–10 days post-eclosion flies were used. Experiments were performed in a custom-built, fully automated apparatus (Bielopolski et al., 2019; Claridge-Chang et al., 2009; Parnas, Lin,



TABLE 1 Key resources

Reagent type (species) or resource	Designation	Source or reference	Identifiers	Additional information
Genetic reagent ( <i>D. melanogaster</i> )	w1118			
Genetic reagent ( <i>D. melanogaster</i> )	<i>zyd</i> <sup>1</sup>	(Melom & Littleton, 2013)		<i>zyd</i>
Genetic reagent ( <i>D. melanogaster</i> )	repo-Gal4	(Lee & Jones, 2005)		
Genetic reagent ( <i>D. melanogaster</i> )	GMR85G01-Gal4	(Kremer, et al., 2017)	RRID:BDSC_40436	Perineurial glia
Genetic reagent ( <i>D. melanogaster</i> )	GMR54C07-Gal4	(Kremer, et al., 2017)	RRID:BDSC_50472	Subperineurial glia
Genetic reagent ( <i>D. melanogaster</i> )	GMR54H02-Gal4	(Kremer, et al., 2017)	RRID:BDSC_45784	Cortex glia
Genetic reagent ( <i>D. melanogaster</i> )	GMR77A03-Gal4	(Kremer, et al., 2017)	RRID:BDSC_39944	Cortex glia
Genetic reagent ( <i>D. melanogaster</i> )	GMR86E01-Gal4	(Kremer, et al., 2017)	RRID:BDSC_45914	Astrocytes
Genetic reagent ( <i>D. melanogaster</i> )	GMR56F03-Gal4	(Kremer, et al., 2017)	RRID:BDSC_39157	Neuropile ensheathing glia
Genetic reagent ( <i>D. melanogaster</i> )	GMR75H03-Gal4	(Kremer, et al., 2017)	RRID:BDSC_39908	Tract ensheathing glia
Genetic reagent ( <i>D. melanogaster</i> )	Moody-Gal4		A gift from Dr. Andrea Brand	
Genetic reagent ( <i>D. melanogaster</i> )	46F-Gal4		A gift from Dr. Vanessa Auld	
Genetic reagent ( <i>D. melanogaster</i> )	Gli-Gal4		A gift from Dr. Vanessa Auld	
Genetic reagent ( <i>D. melanogaster</i> )	Nrv2-Gal4		A gift from Dr. Vanessa Auld	
Genetic reagent ( <i>D. melanogaster</i> )	Alarm-Gal4		RRID:BDSC_67031 RRID:BDSC_67032	
Genetic reagent ( <i>D. melanogaster</i> )	NP2222-Gal4	(Hayashi, et al., 2002)	RRID:DGGR_112830	
Genetic reagent ( <i>D. melanogaster</i> )	Elav-Gal80	(Yang, et al., 2009)		
Genetic reagent ( <i>D. melanogaster</i> )	UAS-dStim-RNAi	Verified in (Petersen, Wolf, & Smyth, 2020)	RRID:BDSC_27263	dStim <sup>RNAi#1</sup>
Genetic reagent ( <i>D. melanogaster</i> )	UAS-dStim-RNAi		RRID:BDSC_41759	dStim <sup>RNAi#2</sup>
Genetic reagent ( <i>D. melanogaster</i> )	UAS-dStim-RNAi		RRID:BDSC_51685	dStim <sup>RNAi#3</sup>
Genetic reagent ( <i>D. melanogaster</i> )	UAS-dStim-RNAi		RRID:BDSC_52911	dStim <sup>RNAi#4</sup>
Genetic reagent ( <i>D. melanogaster</i> )	UAS-dStim-RNAi		RRID:FlyBase_FBst0478081	dStim <sup>RNAi#5</sup>
Genetic reagent ( <i>D. melanogaster</i> )	UAS-Orai-RNAi		RRID:FlyBase_FBst0450445	Orai <sup>RNAi#1</sup>
Genetic reagent ( <i>D. melanogaster</i> )	UAS-Orai-RNAi	Verified in (Petersen, et al., 2020)	RRID:BDSC_53333	Orai <sup>RNAi#2</sup>
Genetic reagent ( <i>D. melanogaster</i> )	UAS-SERCA-RNAi		RRID:FlyBase_FBst0465735	SERCA <sup>RNAi#1</sup>
Genetic reagent ( <i>D. melanogaster</i> )	UAS-SERCA-RNAi		RRID:FlyBase_FBst0479267	SERCA <sup>RNAi#2</sup>
Genetic reagent ( <i>D. melanogaster</i> )	UAS-IP <sub>3</sub> R-RNAi	Verified in (Kohn et al., 2015)	RRID:FlyBase_FBst0451656	ltpR <sup>RNAi#1</sup>
Genetic reagent ( <i>D. melanogaster</i> )	UAS-IP <sub>3</sub> R-RNAi	Verified in (Kohn, et al., 2015)	RRID:FlyBase_FBst0470335	ltpR <sup>RNAi#1</sup>
Genetic reagent ( <i>D. melanogaster</i> )	UAS-IP <sub>3</sub> R-RNAi		RRID:BDSC_51686	ltpR <sup>RNAi#2</sup>
Genetic reagent ( <i>D. melanogaster</i> )	UAS- IP <sub>3</sub> R -RNAi		RRID:BDSC_51795	ltpR <sup>RNAi#3</sup>
Genetic reagent ( <i>D. melanogaster</i> )	UAS- RyR -RNAi		RRID:BDSC_65885	RyR <sup>RNAi#1</sup>

TABLE 1 (Continued)

Reagent type (species) or resource	Designation	Source or reference	Identifiers	Additional information
Genetic reagent ( <i>D. melanogaster</i> )	UAS- RyR -RNAi		RRID:BDSC_31540	RyR <sup>RNAi#2</sup>
Genetic reagent ( <i>D. melanogaster</i> )	UAS- RyR -RNAi		RRID:BDSC_29445	RyR <sup>RNAi#3</sup>
Genetic reagent ( <i>D. melanogaster</i> )	UAS-TRPA	(Zhang, et al., 2017)		
Genetic reagent ( <i>D. melanogaster</i> )	UAS-Chr2 <sup>XXL</sup>	(Dawydow et al., 2014)		
Genetic reagent ( <i>D. melanogaster</i> )	UAS-Shi <sup>ts</sup>		RRID:BDSC_66600	Shi <sup>ts</sup>
Genetic reagent ( <i>D. melanogaster</i> )	UAS-inx1-RNAi		RRID:BDSC_55601	Inx1 <sup>RNAi</sup>
Genetic reagent ( <i>D. melanogaster</i> )	UAS-inx2-RNAi		RRID:BDSC_42645	Inx2 <sup>RNAi#1</sup>
Genetic reagent ( <i>D. melanogaster</i> )	UAS-inx2-RNAi		RRID:BDSC_80409	Inx2 <sup>RNAi#2</sup>
Genetic reagent ( <i>D. melanogaster</i> )	UAS-inx1DN		A gift from Dr. Andrea Brand	Inx1 <sup>DN</sup>
Genetic reagent ( <i>D. melanogaster</i> )	UAS-inx2DN		A gift from Dr. Andrea Brand	Inx2 <sup>DN</sup>
Genetic reagent ( <i>D. melanogaster</i> )	Tub-Gal80 <sup>ts</sup>		RRID:BDSC_7018 RRID:BDSC_7019	
Genetic reagent ( <i>D. melanogaster</i> )	UAS-IVS-mCD8::GFP		RRID:BDSC_32186	mCD8::GFP
Genetic reagent ( <i>D. melanogaster</i> )	UAS-Esyt2::mCherry	(Kikuma, et al., 2017)	RRID:BDSC_77130	Esyt2::mCherry
Genetic reagent ( <i>D. melanogaster</i> )	C155-Gal4 Elav-Gal4		RRID:BDSC_458 RRID:BDSC_8760	
Chemical compound	Dextran	Sigma Aldrich	#30024	1 mM
Chemical compound	Thapsigargin	Sigma Aldrich	#T9033	10 μM
Antibody	Mouse monoclonal anti-repo	DHSB	RRID:AB_528448	1:50
Antibody	Rat monoclonal anti-elav	DHSB	RRID:AB_528218	1:100
Antibody	Rabbit polyclonal antiGFP-488	Invitrogen	#A21311 RRID:AB_221477	1:500
Antibody	DyLight 649 conjugated anti-HRP (horseradish peroxidase)	Jackson ImmunoResearch	#123-605-021	1:2000
Antibody	Goat polyclonal anti-Mouse405	Life technologies	#A31553 RRID:AB_221604	1:3000
Antibody	Goat polyclonal anti-Rat555	Invitrogen	#A21434 RRID:AB_2535855	1:3000
Reagent	EZ-RNA II kit	Biological Industries, Israel	#20-410-100	
Reagent	High-Capacity cDNA Reverse Transcription Kit with RNase Inhibitor	Thermo Scientific	AB-4374966	
Reagent	Fast SYBR <sup>®</sup> Green Master Mix	Applied Biosystems	AB-4385612	
Reagent	Vectashield	Vector Laboratories	RRID:AB_2336789	



Huetteroth, & Miesenbock, 2013; Rozenfeld, Lerner, & Parnas, 2019). Single flies were placed in clear polycarbonate chambers with a constant air flow (3 L/min) that was controlled with mass flow controllers (CMOSens PerformanceLine, Sensirion). The air flow was split between 20 chambers resulting in a flow rate of 0.15 L/min per chamber. The 20 chambers were stacked in two columns each containing 10 chambers and were backlit by 940 nm LEDs (Vishay TSAL6400). Images were obtained by a MAKO CMOS camera (Allied Vision Technologies) equipped with a Computer M0814-MP2 lens. The apparatus was operated in a temperature-controlled incubator (Panasonic MIR 154) at 25°C. A virtual instrument written in LabVIEW 7.1 (National Instruments) extracted fly position data from video images. Data were analyzed in MATLAB 2018a (The MathWorks).

### 2.3 | Immunocytochemistry and structural imaging

3<sup>rd</sup> instar wandering larvae were reared at 25°C and dissected in hemolymph-like HL3.1 solution (70 mM NaCl, 5 mM KCl, 4 mM MgCl<sub>2</sub>, 10 mM NaHCO<sub>3</sub>, 5 mM trehalose, 115 mM sucrose, and 5 mM HEPES, pH 7.2). Larvae were fixed for 45 min in HL3.1 buffer containing 4% paraformaldehyde and washed 3 times for 20 min with PBT (PBS containing 0.1% Triton X-100), followed by a 2 h incubation in block solution (5% NGS in PBT). Samples were incubated overnight at 4°C and washed with two short washes and three extended 20 min washes in PBT, and then incubated with secondary antibodies at room temperature for 2 h or at 4°C overnight. Finally, larvae were rewashed and mounted in Vectashield for imaging. Antibodies used for this study include the following: anti-repo, anti-elav, anti-RFP, DyLight 649 conjugated anti-HRP (horseradish peroxidase), anti-GFP Alexa Fluor 488. Immunoreactive proteins were imaged on either a ZEISS LSM 800 microscope with Airyscan using a 63X oil immersion objective or a Leica TCS SP5 using a 20X oil immersion objective. Images were processed using ImageJ.

### 2.4 | RNA purification, cDNA synthesis, and quantitative real-time PCR analysis

Total RNA from 60 adult heads was extracted using EZ-RNA II kit (Biological Industries, Israel) for each biological replicate. Reverse transcription of total RNA (1000 ng) into complementary DNA (cDNA) was performed using High-Capacity cDNA Reverse Transcription Kit with RNase Inhibitor (Thermo Scientific). qRT-PCR reactions were

performed using Fast SYBR<sup>®</sup> Green Master Mix (Applied Biosystems) in a StepOnePlus instrument (Applied Biosystems). Primers (Table 2) were calibrated, and negative control was performed for each primer pair. Samples measured in technical triplicates and values normalized according to mRNA levels of an RPS3 or  $\beta$ -Tubulin housekeeping genes. The amplification cycles were 95°C for 30 s, 60°C for 15 s, and 72°C for 10 s. At the end of the assay, a melting curve was constructed to evaluate the specificity of the reaction. The fold change for each target was subsequently calculated by comparing to the normalized value of either Elav-Gal4 parent or repo-Gal4. Quantification was assessed at the logarithmic phase of the PCR reaction using the 2<sup>- $\Delta\Delta$ CT</sup> method, as described previously (Livak & Schmittgen, 2001). For the complete dataset, see Table S1.

### 2.5 | Electrophysiology

Intracellular recordings of wandering 3<sup>rd</sup> instar male larvae were performed in HL3.1 saline (in mM: 70 NaCl, 5 KCl, 4 MgCl<sub>2</sub>, 1.5 CaCl<sub>2</sub>, 10 NaHCO<sub>3</sub>, 5 Trehalose, 115 sucrose, 5 HEPES-NaOH, pH 7.2) using an Axoclamp 2B amplifier (Molecular Devices) at muscle fiber 6/7 of segments A3-A5. For recording CPG output, the CNS and motor neurons were left intact. The temperature was controlled with a Peltier heating device and continually monitored with a microprobe thermometer.

### 2.6 | In vivo Ca<sup>2+</sup> imaging

Cyto::GCaMP6s, myr::GCaMP6s, and ER::GCaMP6f were expressed in PG cells using the drivers described above. PG-Gal4 and UAS-myr::GCaMP6s was used for most experiments, except for imaging in RNAi knockdowns (PG > dStim<sup>RNAi</sup> and PG > Orai<sup>RNAi</sup>) where PG-lexA and LexAop-myr::GCaMP6s was used. For live imaging of undissected 2<sup>nd</sup> instar larvae, animals were washed with PBS and placed on a glass slide with a small amount of Halocarbon oil #700 (LabScientific). Larvae were turned ventral side up and gently pressed with a coverslip and a small iron ring to inhibit movement. Under these experimental conditions, Ca<sup>2+</sup> activity was recorded from a ventral view of the VNC, through the larval cuticle, as the dorsal surface of the VNC is not accessible for imaging. For imaging of semi-dissected brains and VNCs, 3<sup>rd</sup> instar larvae were dissected in HL3.1 saline (in mM: 70 NaCl, 5 KCl, 4 MgCl<sub>2</sub>, 0.2 CaCl<sub>2</sub>, 10 NaHCO<sub>3</sub>, 5 Trehalose, 115 sucrose, 5 HEPES-NaOH, pH 7.2). A small incision was made above the brain,

Gene name	Forward primer	Reverse primer
RPS3	ATGAATGCGAACCTTCCGATT	TGATCTCAGTGCGAGAGGGG
$\beta$ -Tubulin	CCAAGGGTCATTACACAGAGG	ATCAGCAGGGTTCACATAACC
dStim	CCAGCTTGCATCGTCAGCTA	TCCTCCCGCAAAAAGTCATCG
Orai	TCTTCTGACCTCATCTGCGTA	GCGTTCGTATAGACACCACATT
RyR	AAGACAGCTCGTGCATCCG	CTGTTTCTCCTCGTGCTCCAT

**TABLE 2** Primers used for qRT-PCR analysis

with the rest of the organs left largely intact. Under these experimental conditions,  $\text{Ca}^{2+}$  activity was recorded from a dorsal view of the brain and VNC. Images were acquired with a PerkinElmer Ultraview Vox spinning disk confocal microscope and a high-speed EM CCD camera at 8–12 Hz with a 20 $\times$  water-immersion objective using Volocity Software. Single optical planes on the surface or a mid-section of the ventral nerve cord (VNC) or brain hemisphere were imaged. Due to frequent movements in RNAi knockdown animals, only brain-PG were used for comparative analysis.

## 2.7 | $\text{Ca}^{2+}$ imaging analysis

Both region-of-interest (ROI)-dependent and event-dependent signal detection methods were used for analysis.  $\text{Ca}^{2+}$  oscillations were analyzed within the first 4 min of imaging at room temperature. Maximal myr::GCaMP6s signals in PG cells were quantified in the central thoracic and abdominal segments of the VNC and the brain. For ROI-dependent analysis, ROIs were manually assigned to avoid regions containing non-perineurial glial cells (i.e. midline glia and neurons, see Figure S2, Figure S5A) based on morphology. Selected ROIs were circular with a 10  $\mu\text{m}$  diameter, except for ROIs at the VNC where the diameter was 20  $\mu\text{m}$ . For single-event detection imaging, data were processed using Astrocyte Quantitative Analysis (AQuA, run on MATLAB GUI, [Wang et al., 2019]). Default parameters were used with the following modifications: for all data sets the detection threshold (*thrARScI*), the temporal cut threshold (*thrTWScl*), and the Rising time uncertainty (*cRise*) were set to 3. In addition, as  $\text{Ca}^{2+}$  imaging at the VNC displayed higher noise levels, a stronger smoothing (*smoXY*) of 0.8 was used. The frequency (temporal density) of events was calculated by dividing the number of detected events that share a spatial footprint and a similar size (Network-Temporal density with similar size only) by the duration of the imaging session.

## 2.8 | Blood–brain-barrier permeability assay

3<sup>rd</sup> instar larval brains were dissected in HL3.1 and incubated with Alexa fluor 647-conjugated 10 Kd dextran (Sigma Aldrich #30024) for 5 min before image acquisition. Brains were then fixed in 4% PFA in PBS for 5 min, washed briefly in PBS, mounted in VectaShield H-1000 (Vector Laboratories) and imaged by confocal microscopy. Sub-perineurial knockdown of Su(H) was used as a positive control in each batch.

## 2.9 | Statistical analysis

All statistical analyses were performed using GraphPad Prism as described in the figure legends. No statistical methods were used to predetermine sample size. All *n* numbers represent biological replicates. Data were pooled from 2 to 3 independent experiments.  $\text{Ca}^{2+}$  imaging experiments were randomized and blinded. Students' *t* test,

One-wat ANOVA and Two-way ANOVA were used, and *p*-values are represented as \* = *p* < 0.05, \*\* = *p* < 0.01, \*\*\* = *p* < 0.001, \*\*\*\* = *p* < 0.0001. *p* < 0.05 was considered significant. Data are expressed as mean  $\pm$  SEM or the median.

## 3 | RESULTS

### 3.1 | Knockdown of glial dStim increases seizure susceptibility

We recently observed that chronic  $\text{Ca}^{2+}$  increase in cortex glia predisposes animals to stimulation-induced seizures (Weiss, et al., 2019), while acute increases in intracellular  $\text{Ca}^{2+}$  in astrocyte-like glia drives neuronal silencing and paralysis (Zhang, et al., 2017), demonstrating key roles for two *Drosophila* glial cell populations in modulating neuronal excitability. To identify additional glial signaling pathways that modulate neuronal excitability, we performed a genetic screen using the pan-glial driver repo-Gal4 to drive expression of RNA interference (RNAi) constructs targeting ~850 genes encoding membrane receptors, secreted ligands, ion channels and transporters, vesicular trafficking proteins and known cellular  $\text{Ca}^{2+}$  homeostasis and  $\text{Ca}^{2+}$  signaling pathway components (Weiss, et al., 2019). This screen revealed that pan-glial knockdown of dStim led to severe HS-induced seizures-like episodes (Video S1, middle, hereafter referred to as seizures), similar to those we previously identified in *NCKX<sup>zvd</sup>* (*zvd*) mutants that disrupt a  $\text{Ca}^{2+}$  ion exchanger in cortex glia (Figure 1(b)) (Melom & Littleton, 2013; Weiss, et al., 2019). Pan-glial knockdown of dStim (repo > dStim<sup>RNAi</sup>) on the *zvd* mutation background led to ~30% of flies showing room-temperature seizures and enhanced HS-induced seizures (Figure 1(b)), indicating the two manipulations disrupt independent pathways that enhance seizure susceptibility. Recordings of the motor central pattern generator (CPG) output at the larval neuromuscular junction (NMJ) demonstrated that 3<sup>rd</sup> instar repo > dStim<sup>RNAi</sup> larvae lose normal rhythmic firing at 38°C and instead display continuous neuronal firing, as observed in *zvd* mutants (Figure 1(c)). The seizure phenotype that resulted from dStim knockdown was similar when dStim was targeted using four additional partially overlapping dStim RNAi constructs (Figure S1A). All five dStim<sup>RNAi</sup> lines also showed seizures when exposed to acute mechanical vortex (a phenotype referred to as bang-sensitivity), though to a lesser extent than following a HS (Figure S1B). To test the efficiency of the dStim RNAi construct, we measured the effect of dStim RNAi #1 on expression level using quantitative real-time polymerase chain reaction (qRT-PCR). dStim RNAi strongly reduced dStim levels ( $65 \pm 16.8\%$  decrease relative to repo-Gal4 control, Figure 1(d), Table S1). The actual knockdown effect of dStim RNAi might be stronger, as the remaining expression partially originates from neuronal expression of dStim. For the remaining experiments, we used the dStim RNAi #1 (see Methods).

The seizure phenotype observed from pan-glial knockdown of dStim might result from a developmental role for glial dStim in the CNS. To test for a developmental effect of dStim knockdown, we



conditionally expressed a single copy of dStim RNAi using Gal4/Gal80<sup>ts</sup> (see Methods) only in adult flies. Adult flies reared at the permissive temperature for Gal80<sup>ts</sup> for 3 days (>30°C, to allow dStim RNAi expression) exhibited significantly more seizures, with ~60% of flies displaying seizure phenotypes (Figure 1(e)). dStim, together with the Ca<sup>2+</sup> release-activated Ca<sup>2+</sup> channel protein, Orai, are implicated in the SOCE pathway. Pan-glial knockdown of Orai using two non-overlapping RNAis (repo > Orai<sup>RNAi</sup>) was embryonic lethal, while dStim knockdown was largely viable and showed seizure phenotypes as described above (Figure S1C). To test the efficiency of the Orai RNAi construct, we measured the effect of Orai RNAi #1 on expression levels using qRT-PCR. As pan-glial knockdown of Orai was embryonic lethal, Elav-Gal4 was used to knockdown Orai in neurons. Elav > Orai RNAi animals were viable and displayed no seizures upon exposure to either HS or vortex stimuli. Orai RNAi strongly reduced Orai expression levels (65 ± 13.1% decrease relative to Elav-Gal4 control, Figure 1(d), Table S1). The actual knockdown effect of Orai RNAi might be stronger, as the remaining expression partially originates from glial cells. For the remaining experiments, we used the Orai RNAi #1 (see Methods). Collectively, these results suggest that the SOCE pathway is likely to be essential in glia, regulating neuronal excitability and susceptibility to seizures.

### 3.2 | Knockdown of dStim in Perineurial glial cells increases seizure susceptibility

To further characterize how dStim knockdown contributes to seizure susceptibility, we performed a secondary screen in which dStim was knocked down specifically in different glial subpopulations. For this screen, we used a series of previously described glial drivers (Hayashi et al., 2002; Kremer, Jung, Batelli, Rubin, & Gaul, 2017; Lee & Jones, 2005; Xie & Auld, 2011). Surprisingly, knockdown of dStim in the two glial subpopulations that are best positioned to influence neuronal activity, cortex glia (CG) and astrocyte-like glia (ALG), failed to recapitulate the phenotype of the pan-glial knockdown (Figure 2a<sup>a</sup>). We found that only knockdown of dStim using two different perineurial glia (PG) drivers (46F-Gal4 (Xie & Auld, 2011) and GMR85G01-Gal4 (Kremer, et al., 2017)), could recapitulate the HS induced seizure phenotype (Figure 2(a), (b), Video S1), although only ~85% of PG > dStim<sup>RNAi</sup> flies displayed seizures. The weaker phenotype caused with the PG drivers suggests these drivers may result in a less efficient knockdown of the transcript compared to the pan-glial driver. Co-expressing Dicer-2 with dStim<sup>RNAi</sup> did not enhance the phenotype (Figure 2a<sup>a</sup>), suggesting involvement of dStim function in other glial sub-types as well.

The GMR85G01-Gal4 driver line was previously shown to drive uniform expression in all PG cells of the adult CNS covering the whole brain and ventral nerve chord (VNC) (Kremer, et al., 2017). Similarly, we found the GMR85G01-Gal4 driver line drives uniform expression in all PG cells of the larval CNS (Figure 2(c), S2A), covering the whole brain and VNC (Figure S2B). GMR85G01-Gal4 also drives expression in PG cells of the larval peripheral nervous system (PNS), partially

enwrapping peripheral nerves (Figure S2C), as previously described for PG cells (Stork, et al., 2008). While the expression of the GMR85G01 driver in the larval brain is restricted to the PG sheet (Figure S2A), similar to the observations in the adult CNS (brain and VNC), we found that at the larval VNC it also drives weak expression in glial cells other than PG cells (Figure S2D) and a small subset of neurons (Figure S2E). Nevertheless, our driver screen suggests the seizure phenotype caused by dStim knockdown does not arise from dStim suppression in cell types other than PG, as knock down with other cell-type-specific drivers did not lead to seizures (Figure 2a<sup>a</sup>), and neuronal suppression of dStim knockdown (using Elav-Gal80, Figure 2a<sup>a</sup>) failed to recapitulate the pan-glial knockdown phenotype. For the remaining experiments, we used the GMR85G01-Gal4 driver, hereafter referred to as PG-Gal4.

Recordings of CPG output at the larval NMJ demonstrated that 3<sup>rd</sup> instar PG > dStim<sup>RNAi</sup> larvae lose normal rhythmic firing at 38°C and instead display continuous neuronal firing (Figure 2(e), (e)). Adult PG > dStim<sup>RNAi</sup> exhibited a significant reduction in locomotor activity levels at room temperature (Figure 2(f)). Thus, basal locomotor activity is also impaired, suggesting a homeostatic effect rather than an acute effect that only occurs during HS. Taken together, these results indicate that the role of glial SOCE in neuronal excitability is primarily required in PG cells.

To further characterize the effects of disrupting SOCE, Orai was specifically knocked down in PG cells. Orai knockdown with the PG driver (PG > Orai<sup>RNAi</sup>) was adult lethal with most animals surviving until late pupal stages, thus preventing the characterization of adult animals. 3<sup>rd</sup> instar PG > Orai<sup>RNAi</sup> larvae showed a significant defect in locomotor activity (Figure 2(g)) and HS-induced seizure-like activity when placed at 38°C (Video S2, left). PG > dStim<sup>RNAi</sup> larvae showed similar activity impairment as PG > Orai<sup>RNAi</sup> larvae (Figure 2(g)). To exclude the possibility that a developmental effect of Orai knockdown in PG cells leads to lethality, Orai<sup>RNAi</sup> was conditionally expressed with Gal4/Gal80<sup>ts</sup> (see Methods) only in adult flies. PG > Orai<sup>RNAi</sup>/Gal80<sup>ts</sup> animals reared at 25°C survived to adulthood and showed no HS-induced seizures 1-day post eclosion (Figure 2(h), (l)). However, over the course of several days at 31°C, the majority (~80%) of PG > Orai<sup>RNAi</sup>/Gal80<sup>ts</sup> flies showed progressive loss of motor control and death (Figure 2(h)), with ~35% of the surviving flies displaying seizures after 7 days (Figure 2(l)). These results indicate Orai function in PG cells is crucial for normal brain function. Consistent with the more severe phenotype of Orai knockdown compared to dStim knockdown with repo-Gal4 or PG-Gal4, the temperature threshold for seizures in PG > Orai<sup>RNAi</sup> larvae was significantly lower compared to PG > dStim<sup>RNAi</sup> (Figure S3A). The stronger effect of Orai knockdown might be due to stronger suppression of the SOCE pathway, or due to Orai functioning in a dStim-independent manner (Deb, Pathak, & Hasan, 2016). To reduce the expression of Orai<sup>RNAi</sup> we reared PG > Orai<sup>RNAi</sup> animals at 18°C, which is below the optimal activation temperature of the UAS/Gal4 system (Duffy, 2002). Under these conditions, ~50% of PG > Orai<sup>RNAi</sup> animals survived to adulthood and showed no HS-induced seizures following eclosion. However, flies that were moved to 25°C after eclosion showed HS-induced seizures

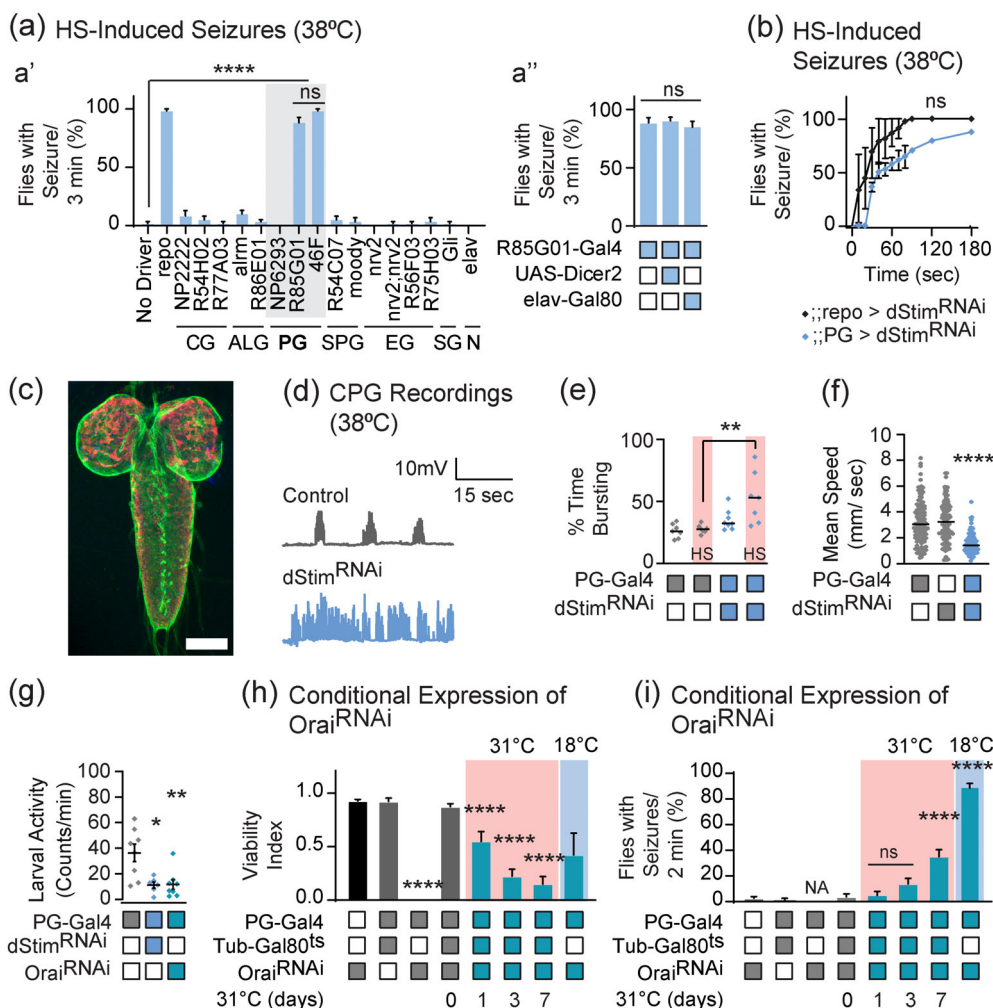


**FIGURE 2** Perineurial knockdown of store-operated  $\text{Ca}^{2+}$  entry pathway (SOCE) components impairs locomotor activity and increases seizure susceptibility. (a) Histograms summarizing the percent of flies exhibiting HS-induced seizures at 3 min (38.5°C). (a') An array of glial specific Gal4 drivers were used to knock down dStim (see methods). Only knockdown of dStim using perineurial glia (PG) drivers (46F-Gal4 and GMR85G01-Gal4) recapitulated the pan-glial HS-induced seizure phenotype ( $p < 0.0001$ , Two-way ANOVA), while knockdown with a third PG driver (NP6293) failed to recapitulate the phenotype. (a'') Inhibiting Gal4 expression of the RNAi in neurons with Gal80 (Elav-Gal80) does not alter the seizures observed with GMR85G01 knockdown, indicating the seizure phenotype does not arise from neuronal knockdown of dStim. Co-expressing Dicer-2 with dStim RNAi (to enhance the knockdown) using the GMR85G01 driver does not enhance the seizure phenotype ( $p > 0.05$ , Two-way ANOVA,  $N = 4$  groups of  $>10$  flies/genotype, error bars are mean  $\pm$  SEM). (b) Time course of heat-shock induced seizures (38.5°C, HS) for  $\text{repo} > \text{dStim}^{\text{RNAi}}$  and  $\text{PG} > \text{dStim}^{\text{RNAi}}$  are shown ( $p > 0.05$ , Two-way ANOVA,  $N = 4$  groups of 20 flies/genotype, error bars are mean  $\pm$  SEM, Video S1). (c) Expression pattern of the perineurial glial driver GMR85G01. GMR85G01 expression of a membrane tethered GFP (mCD8::GFP) reveals high expression in PG cells that enclose the entire larval CNS (brain and VNC); 98  $\mu\text{m}$  projection, scale bar = 100  $\mu\text{m}$  (green: mCD8::GFP, cell membranes; red: anti-elav, neuronal nuclei). For complete expression analysis see Figure S2. GMR85G01 hereafter referred to as PG driver. (d–e) CPG activity in  $\text{PG} > \text{dStim}^{\text{RNAi}}$  showing  $\text{PG} > \text{dStim}^{\text{RNAi}}$  lose normal rhythmic muscle activity under heat-shock (HS) conditions (38°C). (d) Representative voltage traces of spontaneous CPG activity recorded at larval 3<sup>rd</sup> instar muscle 6 at 38°C in control and  $\text{PG} > \text{dStim}^{\text{RNAi}}$  animals ( $n \geq 5$  preparations/genotype). (e) Quantification of percent muscle potential bursting for CPG recordings of  $\text{PG} > \text{dStim}^{\text{RNAi}}$  animals at room temperature and 38°C HS (marked with pink shadings) ( $p < 0.01$ , Student's  $t$  test,  $n \geq 5$  preparations/genotype). (f, g) Activity level of adults (f) and 3<sup>rd</sup> instar larvae (g) expressing dStim RNAi using the PG driver show significant reduction in total locomotor activity ( $p < 0.0001$  for adult flies,  $p < 0.05$ ,  $p < 0.01$  for larvae, Student's  $t$  test,  $N = 8$  larvae/genotype,  $N > 100$  adult flies/genotype, median is presented). (h, i) Perineurial conditional knockdown of Orai using Gal4/Gal80<sup>ts</sup>. Rearing adult flies at the restrictive temperature for Gal80<sup>ts</sup> ( $>30^\circ\text{C}$ , marked with pink shadings) allows expression of Orai<sup>RNAi</sup> only in adults ( $N = 4$  groups of 20 flies/condition, error bars are mean  $\pm$  SEM).  $\text{PG} > \text{Orai}^{\text{RNAi}}$  animals that were reared at 18°C to suppress Gal4-driven transgene expression (marked with blue shading), displayed higher survival rate. (g) Over the course of several days at 31°C, the majority of  $\text{PG} > \text{Orai}^{\text{RNAi}}/\text{Gal80}^{\text{ts}}$  flies died ( $\sim 80\%$  mortality after 7 days,  $p < 0.0001$ , two-way ANOVA). (h) A significant increase in seizures ( $p < 0.0001$ , Two-way ANOVA) was seen after 7 days of rearing flies at the restrictive temperature for Gal80<sup>ts</sup> (31°C). Approximately 30% of surviving adults showed seizures and the rest displayed severe locomotor defects.  $\text{PG} > \text{Orai}^{\text{RNAi}}$  animals that were reared at 18°C to suppress Gal4-driven transgene expression (marked with blue shading), displayed increased seizure susceptibility. \* =  $p < 0.05$ , \*\* =  $p < 0.01$ , \*\*\*\* =  $p < 0.0001$



1 day later (~80%, Figure 2(h), (l), Video S2). Over the course of several days at 25°C, the majority (~80%) of PG > Orai<sup>RNAi</sup>/Gal80<sup>ts</sup> flies rapidly deteriorated and died. To further support the role of ER-originated Ca<sup>2+</sup> signaling in PG cells, we knocked down other central components of ER-related Ca<sup>2+</sup> signaling. While knockdown of the inositol 1,4,5-trisphosphate receptor (IP<sub>3</sub>R) was viable (Figure S3B) and showed no apparent behavioral phenotype (Figure S3C), knockdown of SERCA (Sarco/Endoplasmic reticulum Ca<sup>2+</sup>-ATPase) was adult lethal (Figure S3B). Collectively, these results suggest a critical requirement for ER-related Ca<sup>2+</sup> signaling in PG cells, independent of IP<sub>3</sub>R, that is necessary to maintain normal brain function.

### 3.3 | Knockdown of dStim in perineurial glial cells does not affect blood–brain-barrier integrity

PG cells are thought to influence the development, integrity and function of the blood–brain-barrier (BBB) formed by the SPG layer, as suggested for astrocytes in the mammalian CNS (Abbott, Ronnback, & Hansson, 2006). Perineurial glia also contribute to the deposition of the neural lamella, thus participating in regulating brain shape and stiffness. Alterations in the neural lamella can disrupt brain shape and migration of PG cells (Yildirim, et al., 2019). Hence, alteration of PG Ca<sup>2+</sup> signaling in dStim and Orai knockdowns could lead to seizures secondary to a role for PG ER-related Ca<sup>2+</sup> signaling in controlling brain development. However, this seems unlikely given conditional knockdown of dStim or Orai in adult flies recapitulates the seizure phenotype (Figures 1(e) and 2(l)). Nevertheless, to test for an effect of glial SOCE on brain development and PG migration, we co-expressed dStim<sup>RNAi</sup> or Orai<sup>RNAi</sup> together with mCD8::GFP specifically in PG cells, as done previously (Speder & Brand, 2014). We found no apparent changes between control, PG > dStim<sup>RNAi</sup> and PG > Orai<sup>RNAi</sup> animals in brain wrapping by PG or in brain size of 3<sup>rd</sup> instar larvae (Figure S3D). To test whether PG SOCE knockdown compromises the function of the BBB, we incubated PG > dStim<sup>RNAi</sup> brains with Alexa647-conjugated 10kD dextran and monitored brain penetration of the dye. In both parental control and PG > dStim<sup>RNAi</sup> brains, fluorescent dextran remained at the periphery of the brain (Figure S3E, arrowheads), indicating dStim knockdown does not grossly alter the permeability of the BBB, while in SPG > Su(H)<sup>RNAi</sup> (positive control), significant uptake of the dye was observed (Figure S3E, right, arrowheads), indicating dysfunction of the BBB in these animals. Taken together, these results suggest that PG knockdown of SOCE does not affect the gross integrity of the *Drosophila* blood–brain barrier.

### 3.4 | Dynamic Ca<sup>2+</sup> transients occur in perineurial glia in vivo

Multiple components of the vertebrate BBB, including astrocytes, show fluctuations in intracellular Ca<sup>2+</sup>. Therefore, we explored whether PG cells that contribute to the *Drosophila* BBB also exhibit fluctuations in

Ca<sup>2+</sup>. To examine in vivo Ca<sup>2+</sup> dynamics in PG cells, we expressed a myristoylated variant of GCaMP6s (myr::GCaMP6s) that tethers it to the plasma membrane to monitor Ca<sup>2+</sup> dynamics in fine processes (Melom & Littleton, 2013; Weiss, et al., 2019) specifically in PG cells. We first performed imaging experiments in live, undissected 2<sup>nd</sup> instar larvae as previously described (Melom & Littleton, 2013). PG expression of myr::GCaMP6s revealed Ca<sup>2+</sup> transients in PG cells at the ventral surface of the ventral nerve cord (VNC, Figure 3(a)–(e) and Video 3A) and in peripheral nerves (Figure 3(f)–(h) and Video 3B).

PG cells that enwrap the VNC (CNS-PG) show Ca<sup>2+</sup> signals that range from small, localized elevations to events that cover large areas (Video 3A). These events recur frequently in the same regions (Figure 3(b),(c),(k)), occasionally spreading as waves across large distances (Figure 3(d),(e)), between neighboring segments, and even across the midline (Figure S4A), suggesting adjacent PG cells can laterally transfer information through Ca<sup>2+</sup> waves. The duration of CNS-PG Ca<sup>2+</sup> transients was  $12.96 \pm 0.59$  s and exhibited a mean  $\Delta F/F$  of  $21.08 \pm 0.9\%$  (Figures 3(l), (j)). In contrast, PG cells that enwrap peripheral nerves (PNS-PG) show fast elevations in Ca<sup>2+</sup> along the whole imaging field (Figure 3(f)–(h) and Video 3B). These transients recur frequently (~4 events/min, Figure 3(k)), with a duration of  $2.32 \pm 0.142$  s and a mean  $\Delta F/F$  of  $49.11 \pm 2.61\%$  (Figure 3(l), (j)). Astrocyte Quantitative Analysis (AQuA, [Wang, et al., 2019]) software for single-event detection recapitulated these observations (for example see Figure S4B, for complete analysis see Figure S4C–E) and revealed that PNS-PG also display small, localized sporadic events dispersed between the large Ca<sup>2+</sup> events (Figure S4F–H). Together, these data indicate PG cells display dynamic Ca<sup>2+</sup> signaling in vivo, with PG cells in the CNS and PNS displaying distinct patterns of Ca<sup>2+</sup> activity.

### 3.5 | Characterization of PG Ca<sup>2+</sup> activity reveals unique signatures in cells that occupy different CNS territories

To examine whether influx of external Ca<sup>2+</sup> underlies the observed Ca<sup>2+</sup> transients, and to minimize muscle contractions, we performed imaging in an external solution containing no added Ca<sup>2+</sup> (i.e. nominal [Ca<sup>2+</sup>]<sub>out</sub>). Under these conditions, analysis of assigned ROIs (see methods and Figure S5A) revealed that the dorsal perineurium enwrapping the VNC (VNC-PG) exhibited robust population-wide Ca<sup>2+</sup> elevations (Video S4, Figures 4(a)), suggesting PG Ca<sup>2+</sup> signaling relies on intracellular Ca<sup>2+</sup> stores rather than extracellular influx. Ca<sup>2+</sup> elevations at the VNC appear to be highly correlated between neighboring ROIs (with an average Pearson correlation of  $r = 0.67 \pm 0.01$ , Figure S5B–D), with only a small dependency on the distance between ROIs (Figure S5E). These larger Ca<sup>2+</sup> elevations spread as waves across the entire VNC (Figure 4(b)) and displayed a mean  $\Delta F/F$  of  $53.63 \pm 1.48\%$  (Figure 4(o)) and duration of  $20.20 \pm 0.95$  s (Figure 4(p)). Single event detection (AQuA) recapitulated these population-wide Ca<sup>2+</sup> elevations (Figure S5E) and revealed that these events spread as waves across the entire VNC (Figure 4(b), Video S4). Furthermore, this analysis revealed that PG cells at the VNC also display more localized Ca<sup>2+</sup> elevations that represent

the majority of VNC-PG activity (over 90% of detected events, Figure 4 (d) and Video S4). Analysis of these two event-populations revealed the duration of wide-spread waves was significantly longer ( $3.44 \pm 0.14$  s longer, Figure 4(e), Figure S5G), while the amplitude was not

significantly different (Figure 4(f)). Analysis of the temporal density of  $\text{Ca}^{2+}$  elevations (see Methods) revealed no significant difference between small events and larger, wide-spread waves ( $\sim 7$  events per minute, Figure 4(g), S5H).

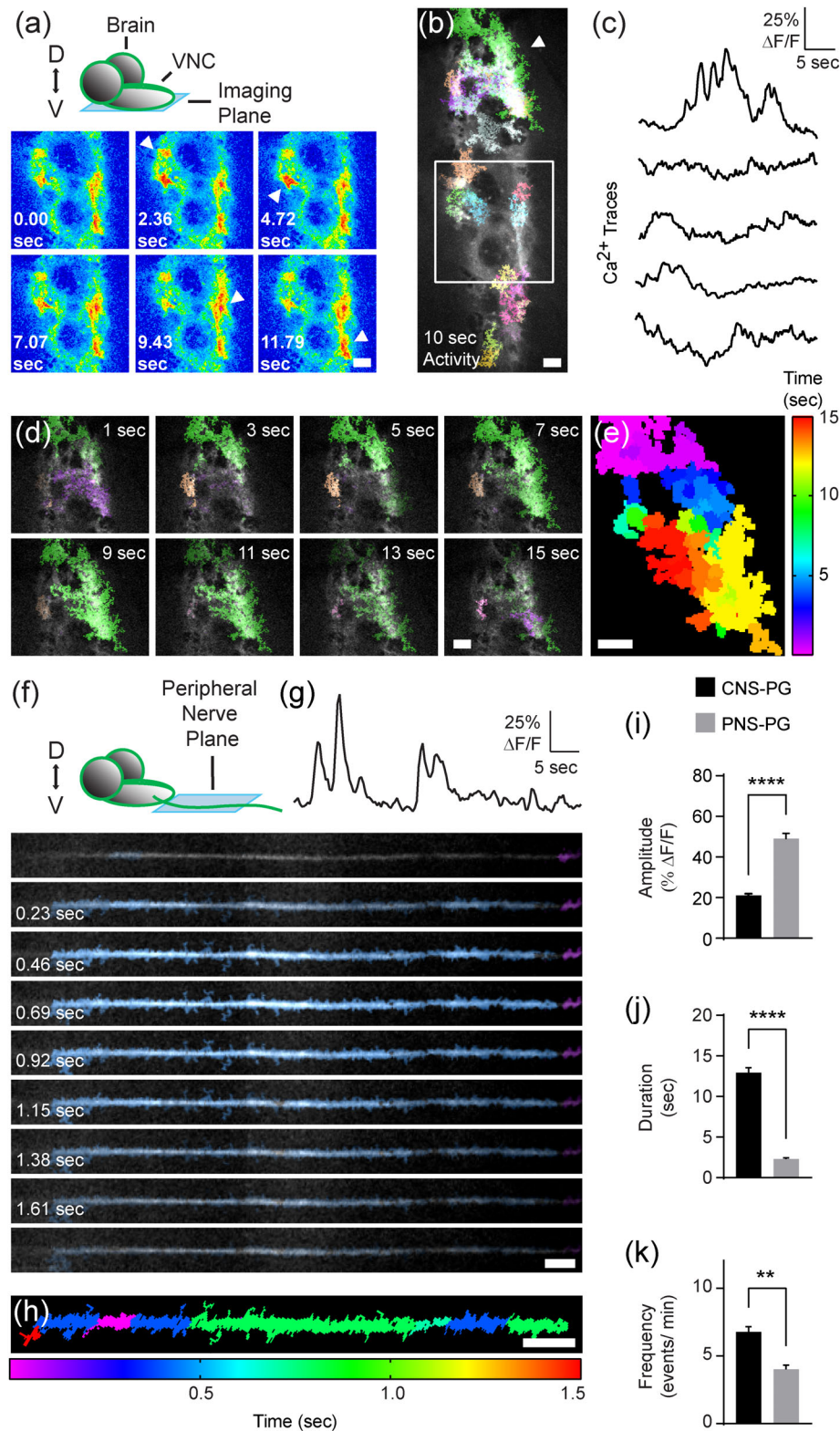


**FIGURE 3** Legend on next page.



The widespread  $\text{Ca}^{2+}$  activity likely represents the activity of multiple PG cells. To characterize the activity of single PG cells, we co-expressed *myr::GCaMP6s* and nuclear *mCherry* (*mCherry.nls*) in PG cells and assigned ROIs to single cells based on nuclear labeling (Video S5, Figures 4(h) and S5I). Single cells at the VNC showed  $\text{Ca}^{2+}$  activity patterns in which cells alternate between active and silent periods (Figure 4(i)). Single-cell activities were mostly asynchronized (with an average *Pearson correlation* of  $r = 0.1926 \pm 0.003$ , Figures 4(j) and S5J, K). The activity of neighboring cells can be more synchronized (Figure S5L), consistent with waves that travel through adjacent cells. The mean duration of single-cell VNC-PG transients was  $20.42 \pm 0.56$  s, similar to what was measured with hemi-segment ROIs (Figure 4(o)).

In contrast to the slow wide-spread waves observed in VNC-PG, the PG sheet on the surface of the brain (Brain-PG) showed fast, asynchronous activity (Video 6A, Figure S6A-C). These transients recurred frequently in the same regions ( $\sim 6$  events/min, Figure S6B). Single event detection revealed that this localized activity occasionally spreads between neighboring cells (Figure S6D, E), however wide-spread waves as observed at the VNC were not detected. Imaging  $\text{Ca}^{2+}$  from a mid-section through a brain hemisphere revealed that brain-PG exhibit  $\text{Ca}^{2+}$  waves that spread through large areas of the PG sheet (Figures 4(k)-(m), Figure S6F and Video 6B, note that sporadic, small events are also visible). These waves recurred frequently in the same regions (Figure S6G) and represent a small fraction of the total brain-PG activity ( $\sim 7\%$  of detected events, Figure 4(n)). Interestingly, the maximum amplitude of these wave events does not necessarily overlap with the initiation site of the event (Figure S6H, I), suggesting these events spread through a propagation mechanism rather than through passive diffusion. Relative to VNC-PG,  $\text{Ca}^{2+}$  waves observed in brain-PG exhibited larger amplitudes, with a mean  $\Delta F/F$  of  $66.38 \pm 2.91\%$  (Figure 4(o)) and shorter duration with a mean duration of  $9.71 \pm 0.26$  s (Figures 4(p)). PNS-PG cells did not show  $\text{Ca}^{2+}$  oscillations under these experimental conditions, suggesting that PNS-PG signaling relies more on extracellular  $\text{Ca}^{2+}$ . Together, these data indicate that PG cells show complex and diverse  $\text{Ca}^{2+}$  activity patterns based on their location, indicating functional diversity within the PG cell population.

### 3.6 | $\text{Ca}^{2+}$ transients in Perineurial glia originate from internal ER $\text{Ca}^{2+}$ stores

The occurrence of PG  $\text{Ca}^{2+}$  transients in a low- $\text{Ca}^{2+}$  external solution suggests that PG  $\text{Ca}^{2+}$  signaling is likely to rely on internal ER  $\text{Ca}^{2+}$  stores. To test this hypothesis, we repeated the  $\text{Ca}^{2+}$  imaging experiments in an external solution containing  $10 \mu\text{M}$  Thapsigargin (Tg, see Methods) to pharmacologically inhibit the restoration of ER  $\text{Ca}^{2+}$  stores. Under these conditions, PG  $\text{Ca}^{2+}$  signaling in both the VNC and the brain is almost completely abolished (Figures 5a and Video 6C). Genetic knockdown of the SOCE pathway is predicted to disrupt restoration of ER  $\text{Ca}^{2+}$  stores and reduce amplitudes of ER-originated  $\text{Ca}^{2+}$  transients. To test this hypothesis, PG  $\text{Ca}^{2+}$  transients were imaged in PG knockdowns of *dStim* and *Orai*. Indeed,  $\text{Ca}^{2+}$  activity of both VNC-PG (Figure 5b) and brain-PG (Figure 5c-h) were significantly reduced (Video S7). Single-event detection revealed that the frequency of  $\text{Ca}^{2+}$  events (Figure 5c), including large-area events ( $>500 \mu\text{m}^2$ , Figure 5d), was significantly lower in SOCE knockdown animals. Furthermore, event area, amplitude, duration and temporal density of the remaining brain-PG activity were significantly reduced in SOCE knockdown animals relative to control (Figure 5e-h). These data indicate that both pharmacological and genetic depletion of ER  $\text{Ca}^{2+}$  stores significantly reduce PG  $\text{Ca}^{2+}$  signaling, supporting the model that PG  $\text{Ca}^{2+}$  activity relies solely on  $\text{Ca}^{2+}$  signals that originate from internal ER  $\text{Ca}^{2+}$  stores.

### 3.7 | Propagation and spread of PG $\text{Ca}^{2+}$ waves through gap junctions are crucial for the prevention of seizures

To examine the role of PG  $\text{Ca}^{2+}$  elevations and PG  $\text{Ca}^{2+}$  waves in the generation of seizures, we artificially elevated  $\text{Ca}^{2+}$  levels in PG cells by over expressing the heat-sensitive  $\text{Ca}^{2+}$  channel TRPA and the light-activated Channel Rhodopsin ( $\text{ChR}^{\text{XXL}}$ ). Activation of

**FIGURE 3** Dynamic  $\text{Ca}^{2+}$  transients occur in Perineurial glia in vivo.  $\text{Ca}^{2+}$  imaging of PG  $>$  *myr::GCaMP6s* in live, non-dissected 2<sup>nd</sup> instar wildtype *Drosophila* larvae. (a) Top, schematic representation of the *Drosophila* larval brain shows the relative field of view at the ventral surface of the VNC (light blue). The dorsal-ventral (D-V) axis is shown. Bottom, time-lapse image series of perineurial glial  $\text{Ca}^{2+}$  at the ventral surface of the VNC (CNS-PG). Arrowheads mark peaks of  $\text{Ca}^{2+}$  transients. Scale bar,  $20 \mu\text{m}$ . (b) 10 second activity projection of PG cells at the ventral side of the VNC, showing  $\text{Ca}^{2+}$  elevations are diverse in size and reoccur in the same regions. Events were detected using single-event detection (AQUA, see methods). The square marks the field of view in panel (a). Arrowhead marks a  $\text{Ca}^{2+}$  wave that is presented in panels D, E. Scale bar,  $20 \mu\text{m}$ . (c) Representative traces of mean fluorescence ( $\% \Delta F/F$ ) in active regions.  $\text{Ca}^{2+}$  elevation in the upper trace is shown in panels (d), (e). (d-e) Slow  $\text{Ca}^{2+}$  waves occur in VNC-PG cells in vivo. (d) Time-lapse image series of a single slow  $\text{Ca}^{2+}$  elevation ( $\sim 15$  sec duration) that spreads as a wave across large distances. (e) Heatmap summarizing the rise time and spread of the wave shown in panel (d). Scale bars,  $20 \mu\text{m}$ . (f-g) Fast  $\text{Ca}^{2+}$  elevations occur in PNS-PG in vivo. (f) Top, schematic representation of the *Drosophila* larval brain shows the relative field of view at a peripheral nerve (light blue). Bottom, time-lapse image series of perineurial glial  $\text{Ca}^{2+}$  signals in an abdominal segment peripheral nerve (PNS-PG). Event-based detection revealed that  $\text{Ca}^{2+}$  elevation in PNS-PG is synchronized across wide areas. Scale bar,  $20 \mu\text{m}$ . (g) Representative trace of the mean fluorescence ( $\% \Delta F/F$ ) of an active region of PNS-PG. (h) Heatmap summarizing the rise time of a single fast event in PNS-PG. Scale bars,  $20 \mu\text{m}$ . (i-k) Histograms comparing  $\text{Ca}^{2+}$  transient characteristics in PG cells of the VNC (CNS-PG) or enwrapping peripheral nerves (PNS-PG). (i) Transient amplitudes are significantly larger in PNS-PG ( $\% \Delta F/F$ ,  $p < 0.0001$ , Student's *t* test,  $n = 99$  transients/23 ROIs/4 VNCs,  $n = 65$  transients/5 nerves/5 animals). (j) Transient durations are significantly shorter for PNS-PG (seconds,  $p < 0.0001$ , Student's *t* test,  $n = 61$  transients/23 ROIs/4 VNCs,  $n = 61$  transients/5 nerves/5 animals). (k) Transient frequencies are significantly lower in PNS-PG (transients/minute,  $p < 0.01$ , Student's *t* test,  $n = 23$  ROIs/4 VNCs,  $n = 5$  nerves/5 animals). \*\* =  $p < 0.01$ , \*\*\*\* =  $p < 0.0001$ .

these channels in PG cells with temperature shifts or light did not alter the PG > dStim<sup>RNAi</sup> seizure phenotype or cause a behavioral phenotype by themselves (Figure S7A), suggesting the phenotype arising from SOCE knockdown is due to an impairment in an ER related signaling pathway rather than from an alteration in basal [Ca<sup>2+</sup>]<sub>i</sub>.

Ca<sup>2+</sup> waves in mammalian astrocytes spread via direct communication between adjoining cells through gap junction channels or by release of gliotransmitters that activate neighboring cells via membrane receptors. These two mechanisms are thought to work in parallel to coordinate Ca<sup>2+</sup> activity between neighboring cells (Scemes & Giaume, 2006). To examine the mechanism that mediates Ca<sup>2+</sup> wave

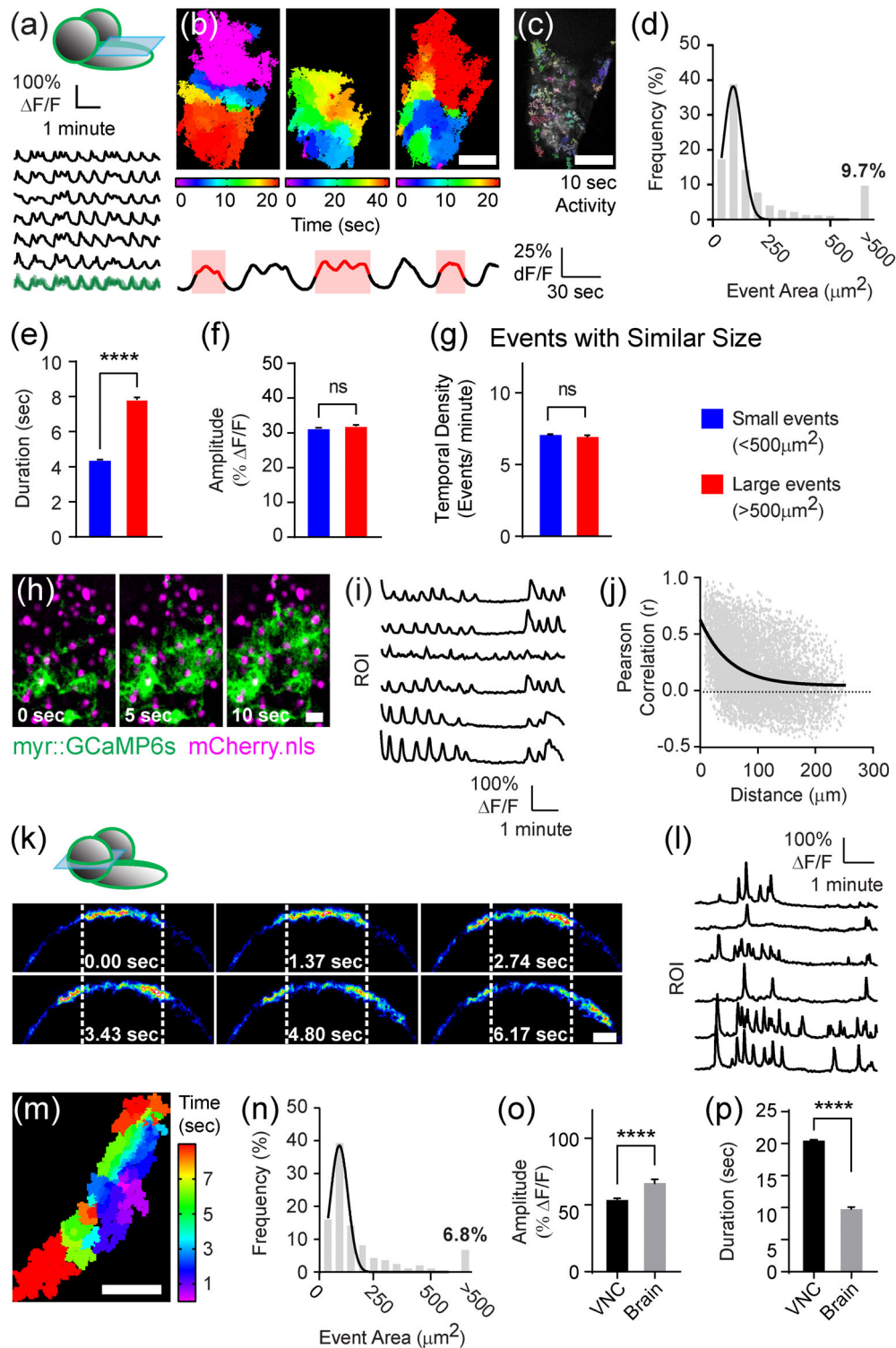


**FIGURE 4** Legend on next page.

spread within the PG cellular sheet, we first manipulated PG secretion by overexpressing the temperature-sensitive (ts) allele of the *Drosophila* Dynamin homolog, Shibire (Shi<sup>ts</sup>). Conditionally inhibiting endocytosis (and subsequent exocytosis) in PG cells, either acutely (by subjecting PG > Shi<sup>ts</sup> flies directly to 38°C) or constitutively (by pre-incubating PG > Shi<sup>ts</sup> flies at the restrictive temperature, 30°C, before a 38°C HS) had no effect on seizure susceptibility of either wildtype or PG > dStim<sup>RNAi</sup> animals (Figure S7B). These results suggest gap junction communication may be the dominant mode of Ca<sup>2+</sup> wave spread in *Drosophila* PG cells rather than through the secretion of exogenous factors.

Within the *Drosophila* BBB, SPG cells exhibit Ca<sup>2+</sup> waves that spread through neighboring SPG cells via gap junctions (Holcroft, et al., 2013; Speder & Brand, 2014). Astrocytes and pericytes at the vertebrate BBB also exhibit Ca<sup>2+</sup> waves that spread through gap junctions (Burdyga & Borysova, 2018). To test whether the spread of Ca<sup>2+</sup> waves between neighboring PG cells is mediated by gap junctions, we over-expressed a dominant-negative (DN) form of one of the *Drosophila* gap junction homologs, Inx2 (Inx2<sup>DN</sup>), in PG cells. PG over-expression of Inx2<sup>DN</sup> significantly inhibited Ca<sup>2+</sup> activity in PG cells in the VNC and the brain (Figure 6a and Video S8). Single-event detection revealed that the total Ca<sup>2+</sup> activity is significantly reduced (Figure 6b,c), although the reduction in the occurrence of large-area events (>500 μm<sup>2</sup>) in Inx2<sup>DN</sup> animals was variable and not significant (Figure 6d). Furthermore, event amplitude and duration of the remaining brain-PG activity were significantly reduced in Inx2<sup>DN</sup>

animals relative to control (Figure 6e-f). Similar to other genetic manipulations described above, RNAi-mediated knockdown of either Inx1 or Inx2, or overexpression of Inx2<sup>DN</sup>, was adult lethal. Conditionally expressing Inx2<sup>DN</sup> with Gal4/Gal80<sup>ts</sup> (see Methods) only in adult flies significantly increased their seizure susceptibility, with ~60% of the flies showing seizures after 15 h at the restrictive temperature for Gal80<sup>ts</sup> (>30°C, Figure 6g, Video S8). Together, these results suggest a key role for gap junctions in the propagation of Ca<sup>2+</sup> waves through adjacent PG cells.

### 3.8 | Ca<sup>2+</sup> signals in perineurial cells occur at ER-Plasma membrane contacts

Astrocytes exhibit highly complex and dynamic fluctuations in Ca<sup>2+</sup> that vary between different cellular compartments (Khakh & Deneen, 2019). To further explore the spread of Ca<sup>2+</sup> activity in PG cells, we used a soluble variant of GCaMP6s (cyto::GCaMP6s). This variant of GCaMP6s did not fill the entire volume of PG cells, and the recorded events displayed small amplitudes and a low signal-to-noise ratio (Figure S7C-D). To capture Ca<sup>2+</sup> activity that occurs proximate to the ER in PG cells, we generated a transgenic *Drosophila* line expressing GCaMP6f tethered to the external surface of the ER ([Niwa, et al., 2016], ER::GCaMP6f, see Methods). We hypothesized that imaging ER-derived Ca<sup>2+</sup> signals in proximity to its source might reveal faster events using the GCaMP6f variant that has

**FIGURE 4** Characterization of PG Ca<sup>2+</sup> reveals distinct signatures in cells that occupy different CNS territories. Imaging of PG > myr::GCaMP6s in dissected 3<sup>rd</sup> instar wildtype *Drosophila* larvae. (a-j) Ca<sup>2+</sup> activity of PG cells at the dorsal surface of the VNC. (a) *Top*, schematic representation of the *Drosophila* larval brain shows the relative field of view at the dorsal surface of the VNC (light blue). *Bottom*, representative traces of the mean fluorescence (% ΔF/F) of manually assigned ROIs (see methods and Figure S5A). (b) *Top*, heatmaps summarizing the rise time and spread of three representative slow waves that occurred in the same region of the VNC. This analysis revealed that waves are highly variable, and do not have a preferable direction of spread. Scale bar, 100 μm. *Bottom*, a whole trace of mean fluorescence (% ΔF/F) summarizing the detected activity. The waves shown in the upper panel are marked with pink shadings. (c) 10 s activity projection showing small Ca<sup>2+</sup> elevations that occur between slow waves. These events reoccur in the same regions. Events were detected using single-event detection (AQuA). Scale bar, 100 μm. (d) Histogram summarizing the frequency (%) of event size (μm<sup>2</sup>). Small events (<500 μm<sup>2</sup>) represent the majority of Ca<sup>2+</sup> activity at the VNC (>90%). The frequency distribution of event size follows a Gaussian distribution, with an R<sup>2</sup> = 0.87. (e-g) Histograms comparing different characteristics of small area events (<500 μm<sup>2</sup>) versus wide-spread Ca<sup>2+</sup> waves (>500 μm<sup>2</sup>). Data were derived from event-based detection (AQuA, see methods). N = 5 animals/4 min imaging session each. Event durations (j) are significantly shorter for small area events (3.44 ± 0.14 seconds shorter, p < 0.0001, Student's t test), while transient amplitudes (e, % ΔF/F) and temporal density of events (g, see methods) are not significantly changed between the two event-populations (Student's t test). (h-j) Ca<sup>2+</sup> activity of single PG cells co-expressing myr::GCaMP6s and nuclear-localized mCherry (magenta: mCherry.nls, PG nuclei; green: myr::GCaMP6s, PG membrane). (h) Time-lapse image series of PG Ca<sup>2+</sup> showing a Ca<sup>2+</sup> wave spreading through multiple adjacent PG cells (also see Video S5). Scale bar, 20 μm. (i-j) Analysis of single cell Ca<sup>2+</sup> activity. ROIs were assigned to single cells by mCherry.nls as shown in Figure S5I. (i) Representative traces of mean myr::GCaMP6s fluorescence (% ΔF/F) of single cells reveal dynamic Ca<sup>2+</sup> activity. (j) Ca<sup>2+</sup> activity of single VNC-PG is mostly asynchronized between single cells across the VNC (also see Figure S5J, K) independently of distances between cells. An exponential fit (R<sup>2</sup> = 0.19) shows a decay of tau = 50.8 μm (n = 228 cells/N = 3 animals). (k-m) Ca<sup>2+</sup> activity of PG cells at the brain (brain-PG). (k) *Top*, schematic representation of the *Drosophila* larval brain shows the relative field of view at a mid-section through a brain hemisphere (light blue). *Bottom*, time-lapse image series of Ca<sup>2+</sup> imaging in PG that enwrap a brain hemisphere (brain-PG). Mid-section is shown. Ca<sup>2+</sup> activity at brain-PG can be localized to small areas or spread as waves across large distances (also see Figure S6F, G and Video S6). (l) Representative traces of mean fluorescence (% ΔF/F) show highly variable dynamic Ca<sup>2+</sup> activity (Video S6). (m) Heatmap summarizing the rise time and spread of a single wide-spread Ca<sup>2+</sup> wave at the brain. This analysis revealed that waves are highly variable, and do not have a preferable direction of spread (see also Figure S6F). Scale bar, 20 μm. (n) Wide-spread Ca<sup>2+</sup> waves (>500 μm<sup>2</sup>) represent only a small fraction of brain-PG Ca<sup>2+</sup> activity (6.8% of the total detected activity). Overall, the frequency distribution of event size follows a Gaussian distribution, with an R<sup>2</sup> = 0.83. (o-p) Comparisons of Ca<sup>2+</sup> transient characteristics in VNC-PG and brain-PG. Data was derived from event-based detection (AQuA, see methods). N = 5 animals/4 min imaging session each/CNS region. Brain-PG transients show significantly higher amplitudes (p < 0.0001, Student's t test) (o) and shorter event durations (p < 0.0001, Student's t test) (p). \*\*\*\* = p < 0.0001

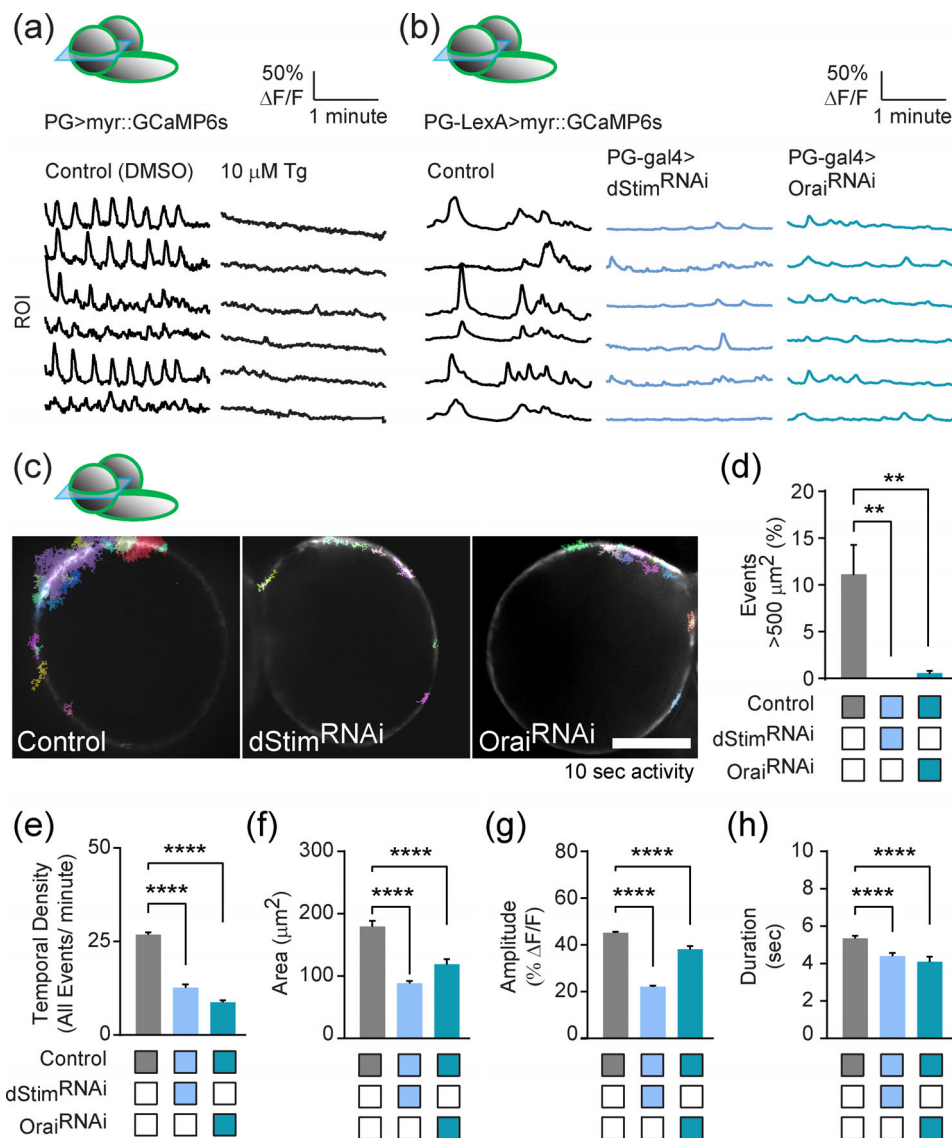


**FIGURE 5** Pharmacologically and Genetically Inhibiting ER  $Ca^{2+}$  Signaling Abolish Perineurial  $Ca^{2+}$  Activity. (a) Pharmacologically inhibiting ER  $Ca^{2+}$  signaling in dissected 3<sup>rd</sup> instar wildtype *Drosophila* larvae. Top, schematic representation of the *Drosophila* larval brain shows the relative field of view at a section through a brain hemisphere (light blue). Bottom, representative traces of mean myr::GCaMP6s fluorescence (%  $\Delta F/F$ ) of randomly assigned ROIs in brain-PG show dynamic  $Ca^{2+}$  activity under control conditions (1% DMSO) that is completely abolished when samples are incubated in 10  $\mu M$  Thapsigargin (Tg) for 2 min prior to imaging. Rapid decrease in basal myr::GCaMP6s fluorescence prevented automated detection of small events. (b-h) Imaging of PG-lexA > LexApo-myr::GCaMP6s following genetic inhibition of SOCE. (b) Top, schematic representation of the *Drosophila* larval brain shows the relative field of view at the dorsal surface of the VNC (light blue). Bottom, representative traces of mean fluorescence (%  $\Delta F/F$ ) in ROIs assigned to VNC hemi-segments show significant reduction in VNC-PG  $Ca^{2+}$  activity in SOCE knockdowns (PG > dStim<sup>RNAi</sup> and PG > Orai<sup>RNAi</sup>, also see Video S7). (c) Top, schematic representation of the *Drosophila* larval brain shows the relative field of view at a mid-section through a brain hemisphere (light blue). Bottom, 10 s activity projection showing the total temporal density of  $Ca^{2+}$  elevations in control, PG > dStim<sup>RNAi</sup> and PG > Orai<sup>RNAi</sup> animals. Events were detected using single-event detection (AQuA, see methods). Scale bar, 100  $\mu m$ . (d-h) Comparisons of  $Ca^{2+}$  transient characteristics in brain-PG of control, PG > dStim<sup>RNAi</sup> and PG > Orai<sup>RNAi</sup> animals. Data was derived from event-based detection (AQuA, see methods).  $N = 5$  animals/4 min imaging session each/ genotype. (d) Brain-PG activity in SOCE knockdown (dStim and Orai RNAis) show significantly less large area events (>400  $\mu m^2$ ,  $p < 0.01$ , One-way ANOVA). Control Brain-PG transients show significantly higher temporal density (e,  $p < 0.0001$ , One-way ANOVA), larger areas and amplitudes (f, g,  $p < 0.0001$ , One-way ANOVA) and longer event durations (h,  $p < 0.0001$ , One-way ANOVA). \*\* $p < 0.01$ , \*\*\*\* =  $p < 0.0001$

faster kinetics. Surprisingly, the recorded events using the myr::GCaMP6s and ER::GCaMP6f sensors were similar (see below), indicating the slow kinetics observed using myr::GCaMP6s was not an artifact.

Imaging  $Ca^{2+}$  activity of brain-PG using ER::GCaMP6f revealed robust activity (Figures 7a, S7E-H and Video S9), with single events showing a similar waveform to that observed with myr::GCaMP6s (Figure 7b). Although GCaMP6f signals are reported to display smaller

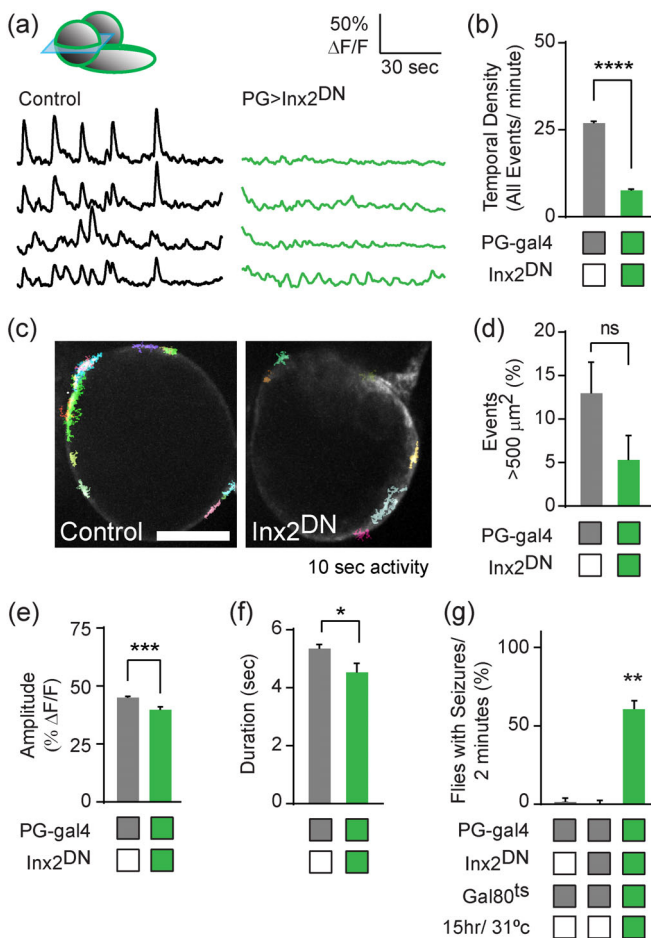


**FIGURE 6**  $\text{Ca}^{2+}$  waves spread is necessary for preventing neuronal hyperexcitability. Imaging of PG > myr::GCaMP6s in dissected 3<sup>rd</sup> instar *Drosophila* larvae expressing *Inx2<sup>DN</sup>*. (a) Top, schematic representation of the *Drosophila* larval brain shows the relative field of view at a mid-section through a brain hemisphere (light blue). Bottom, representative traces of mean myr::GCaMP6s fluorescence (%  $\Delta F/F$ ) show that PG  $\text{Ca}^{2+}$  activity is significantly reduced in PG > *Inx2<sup>DN</sup>* animals compared to control. (b) The total temporal density of  $\text{Ca}^{2+}$  events is significantly reduced in PG > *Inx2<sup>DN</sup>* animals relative to control ( $p < 0.0001$ , Student's *t* test). (c) 10 s activity projection showing the total temporal density of  $\text{Ca}^{2+}$  elevations in control, and PG > *Inx2<sup>DN</sup>* animals. Scale bar, 100  $\mu\text{m}$ . (d-g) Comparisons of  $\text{Ca}^{2+}$  transient characteristics in brain-PG of control and PG > *Inx2<sup>DN</sup>* animals. Data were derived from event-based detection (see methods).  $N = 5$  animals/4 min imaging session each/genotype. Brain-PG activity in *Inx2<sup>DN</sup>* animals show non-significant decrease in wide-spread event occurrence (d,  $>500 \mu\text{m}^2$ ). In contrast,  $\text{Ca}^{2+}$  events in control Brain-PG display significantly higher amplitudes (e,  $p < 0.001$ , Student's *t* test), and longer durations (f,  $p < 0.0001$ , Student's *t* test). (g) Histogram summarizing the percent of flies exhibiting heat-shock induced seizures at 2 min (38.5°C) following conditional PG > *Inx2<sup>DN</sup>* expression only in adult flies. Flies in which *Inx2<sup>DN</sup>* expression was induced for 15 h show enhanced seizures relative to controls ( $p < 0.001$ , Student's *t* test,  $N = 4$  groups of 20 flies/genotype). \* =  $p < 0.05$ , \*\* $p < 0.01$ , \*\*\* =  $p < 0.001$ , \*\*\*\* =  $p < 0.0001$

amplitudes than signals recorded with GCaMP6s (Chen et al., 2013), events recorded using ER::GCaMP6f had significantly larger amplitudes than those observed with membrane-bound myr::GCaMP6s

(mean  $\Delta F/F$  of  $53.02 \pm 2.9\%$ , Figure 7c). This observation suggests PG  $\text{Ca}^{2+}$  events are being recorded close to their source. These  $\text{Ca}^{2+}$  transients recurred frequently in the same regions ( $\sim 3\text{--}4$  events/min, Figure 7a,d), similar to what was observed using myr::GCaMP6s, providing additional support that all events observed in PG cells originate from internal ER  $\text{Ca}^{2+}$  stores. Single event detection revealed that ER::GCaMP6f detected events occasionally spread through several adjacent cells (Figure S7G,H), similar to what we observe for myr::GCaMP6s events (Figure S6D,E). The similar waveforms of the transients measured with ER::GCaMP6f and myr::GCaMP6s together with similar frequencies indicate that the majority of events in PG cells originate from ER  $\text{Ca}^{2+}$  stores.

The observation that activities recorded using myr::GCaMP and ER::GCaMP are similar, suggests PG  $\text{Ca}^{2+}$  activity localizes to ER: plasma membrane (PM) contacts. Together with the low signals recorded with cyto::GCaMP, these data suggest ER accumulates close to the PM to form ER:PM contacts. Indeed, examination of the cellular localization of ER::GCaMP6f in VNC-PG revealed that ER fills the entire cellular volume and accumulates around the nucleus and in the periphery of the cell where PG cell-to-cell contacts are formed (Figure S7I), consistent with a role for ER signaling in cell-to-cell communication. To further confirm this observation, we co-expressed the ER:PM-contact marker *Esyt2* (Giordano et al., 2013) tagged with mCherry (*Esyt2::mCherry*, [Kikuma, Li, Kim, Sutter, & Dickman, 2017]) and a membrane-tethered GFP (*mCD8::GFP*) specifically in PG cells, and found extensive accumulation of *Esyt::mCherry* at cell-to-cell contact sites (Figure 7e). Together, these data indicate PG cells exhibit complex and diverse ER-originated  $\text{Ca}^{2+}$  activity that propagates through adjacent cells to form robust  $\text{Ca}^{2+}$  waves that spread over long distances in the *Drosophila* nervous system.

### 3.9 | RyR mediated perineurial $\text{Ca}^{2+}$ wave propagation is crucial for the prevention of seizures

$\text{Ca}^{2+}$  release from the ER through IP<sub>3</sub>R and/or ryanodine receptors (RyR), is thought to be the major intracellular  $\text{Ca}^{2+}$  mobilization pathway (Bazargani & Attwell, 2016). However, our results suggest ER-related  $\text{Ca}^{2+}$  signaling in PG cells is independent of IP<sub>3</sub>R. Activation of RyR dependent  $\text{Ca}^{2+}$ -induced  $\text{Ca}^{2+}$ -release (CICR) in astrocytes has been observed in response to various stimulations (Hua et al., 2004; Rodriguez-Prados, Rojo-Ruiz, Garcia-Sancho, & Alonso, 2020). As such, RyR-mediated CICR may be the primary mechanism that generates PG  $\text{Ca}^{2+}$  waves and acts to amplify  $\text{Ca}^{2+}$  signaling.

To investigate the role of RyR in PG  $\text{Ca}^{2+}$  waves, we first knocked down RyR using the PG driver. Similar to other genetic manipulations described above, RNAi-mediated knockdown of RyR was adult lethal (either partial or complete lethality, Figure S7J). To test the efficiency of the RyR RNAi, we measured the effect of RyR RNAi #1 on expression levels using qRT-PCR. RyR RNAi strongly reduced RyR expression levels ( $36.47 \pm 0.9\%$  decrease relative to Repo-Gal4 control, Figure S7K, Table S1). Recordings of CPG output at the larval NMJ demonstrated that 3<sup>rd</sup> instar PG > RyR<sup>RNAi</sup> larvae lose normal

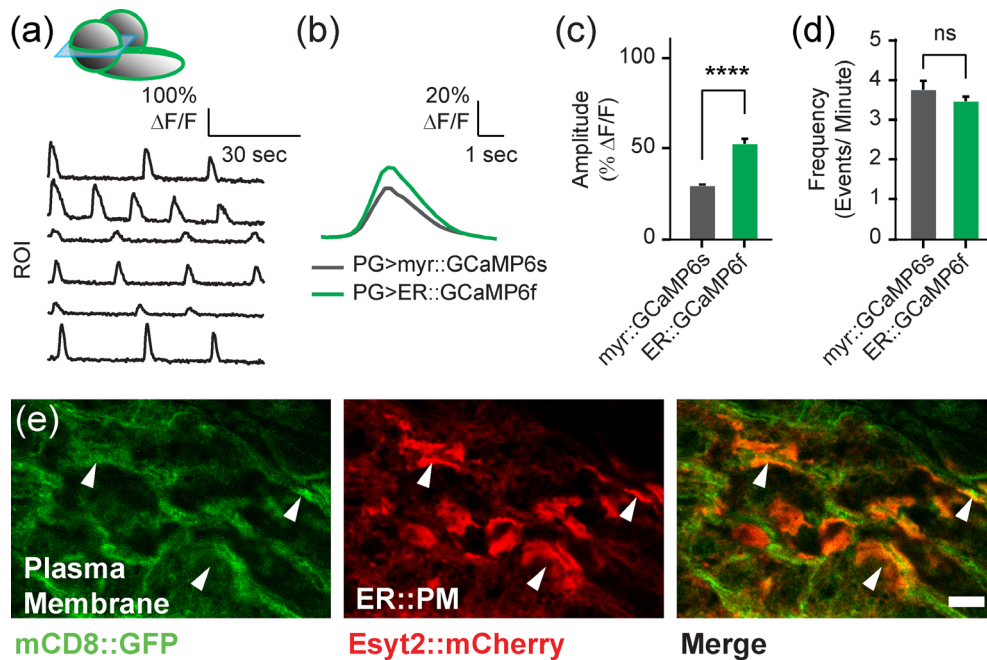


**FIGURE 7** ER originated Ca<sup>2+</sup> waves in PG cells. Imaging of PG > ER::GCaMP6f in dissected 3<sup>rd</sup> instar wildtype *Drosophila* larvae. (a) Top, schematic representation of the *Drosophila* larval brain shows the relative field of view at a section through a brain hemisphere (light blue). Bottom, Representative traces of mean ER::GCaMP6s fluorescence (% ΔF/F) show dynamic Ca<sup>2+</sup> activity. (b-d) myr::GCaMP6s and ER::GCaMP6f Ca<sup>2+</sup> transients in brain-PG reveal similar kinetics. (b) Superimposition of the means of myr::GCaMP6s and ER::GCaMP6f Ca<sup>2+</sup> transients in brain-PG ( $n > 100$  events/ $N = 3$  animals/sensor). (c-d) Comparison of isolated Ca<sup>2+</sup> transient amplitudes (% ΔF/F) recorded with myr::GCaMP6s and ER::GCaMP6f shows significant amplitude increase (c) and similar frequency (d) in ER::GCaMP6f recorded events relative to myr::GCaMP6s ( $p < 0.0001$ , Student's  $t$  test,  $N = 3$  animals/4 min imaging session). (e) Structural imaging of the cellular localization of ER-plasma membrane (ER::PM) contacts in PG cells. The PG driver was used to co-express a plasma membrane tethered GFP (mCD8::GFP) and a mCherry tagged Esyt2 (ESyt2::mCherry, as a marker of ER::PM contacts). Z-stack projection (3 μm) reveals substantial accumulation of Esyt2::mCherry around cell-cell contacts (visible as two parallel membranes marked with GFP, arrowheads). Scale bar, 5 μm. \*\*\*\* =  $p < 0.0001$

rhythmic firing at 38°C (Figure 8(b),(c)), as observed in PG knockdown of dStim (Figure 2(d),(e)). In RyR knockdowns that caused partial lethality, ~40% of PG > RyR<sup>RNAi</sup> flies that survived to adulthood showed HS-induced seizures (Figure 8(c)). Lastly, Ca<sup>2+</sup> imaging (Figure 8(d)) revealed that PG > RyR<sup>RNAi</sup> animals show a significant reduction in the temporal density, size, amplitude and duration of Ca<sup>2+</sup> signals (Figure 8(e)-(j)), and significant inhibition of Ca<sup>2+</sup> wave spread in PG cells (i.e. decrease in the abundance of events larger than 500 μm<sup>2</sup>, Figure 8(g)). Together, these data demonstrate that PG Ca<sup>2+</sup> waves are mediated by RyR-dependent CICR and spread through neighboring cells via gap junctions. Blocking the spread of these Ca<sup>2+</sup> waves recapitulate the behavioral phenotypes of SOCE knockdown, suggesting propagation of PG Ca<sup>2+</sup> waves is crucial for maintaining normal brain excitability and preventing seizure activity.

## 4 | DISCUSSION

Ca<sup>2+</sup> signaling is considered to be essential for astrocyte function (Khakh & Deneen, 2019; Khakh & McCarthy, 2015), with release from intracellular Ca<sup>2+</sup> stores as one of the major underlying mechanisms. Genetic deletion of the inositol 1,4,5-trisphosphate receptor (IP<sub>3</sub>R) type-2 (IP<sub>3</sub>R2), the major IP<sub>3</sub>R expressed in astrocytes, was reported

to eliminate ER Ca<sup>2+</sup> release in astrocytes. However, recent studies have shown the presence of astrocytic Ca<sup>2+</sup> transients in IP<sub>3</sub>R2 knockout mice (Agarwal, et al., 2017; Kanemaru et al., 2014; Rungta et al., 2016; Srinivasan et al., 2015). These IP<sub>3</sub>R2-independent Ca<sup>2+</sup> signals are thought to be mediated by plasma membrane Ca<sup>2+</sup> influx (Rungta, et al., 2016; Shigetomi, et al., 2012; Srinivasan, et al., 2015) or Ca<sup>2+</sup> release from mitochondria (Agarwal, et al., 2017). In contrast to the vast interest in astrocytic IP<sub>3</sub>R related signaling, the role of ryanodine receptors (RyRs) in astrocyte Ca<sup>2+</sup> signaling is largely unstudied and controversial (Rodriguez-Prados, et al., 2020). The expression and function of RyR3 in astrocytes has been reported (Chai et al., 2017; Matyash, Matyash, Nolte, Sorrentino, & Kettenmann, 2002), although the physiologically relevant mechanism for astrocytic RyR activation remains elusive. In this study, we found that genetic manipulations in the ER SOCE pathway in *Drosophila* PG cells leads to severe HS-induced seizures. We performed a detailed characterization of PG Ca<sup>2+</sup> signaling that revealed PG cells exhibit robust Ca<sup>2+</sup> activity. These Ca<sup>2+</sup> transients are independent of extracellular Ca<sup>2+</sup> and originate from internal stores as they are sensitive to Tg, knockdown of RyR, or knockdown of components of the SOCE pathway. We further show that Ca<sup>2+</sup> waves propagating through the glial network via gap junctions are crucial for the generation of single PG cell Ca<sup>2+</sup> transients. Ca<sup>2+</sup> signals in PG cells are essential for

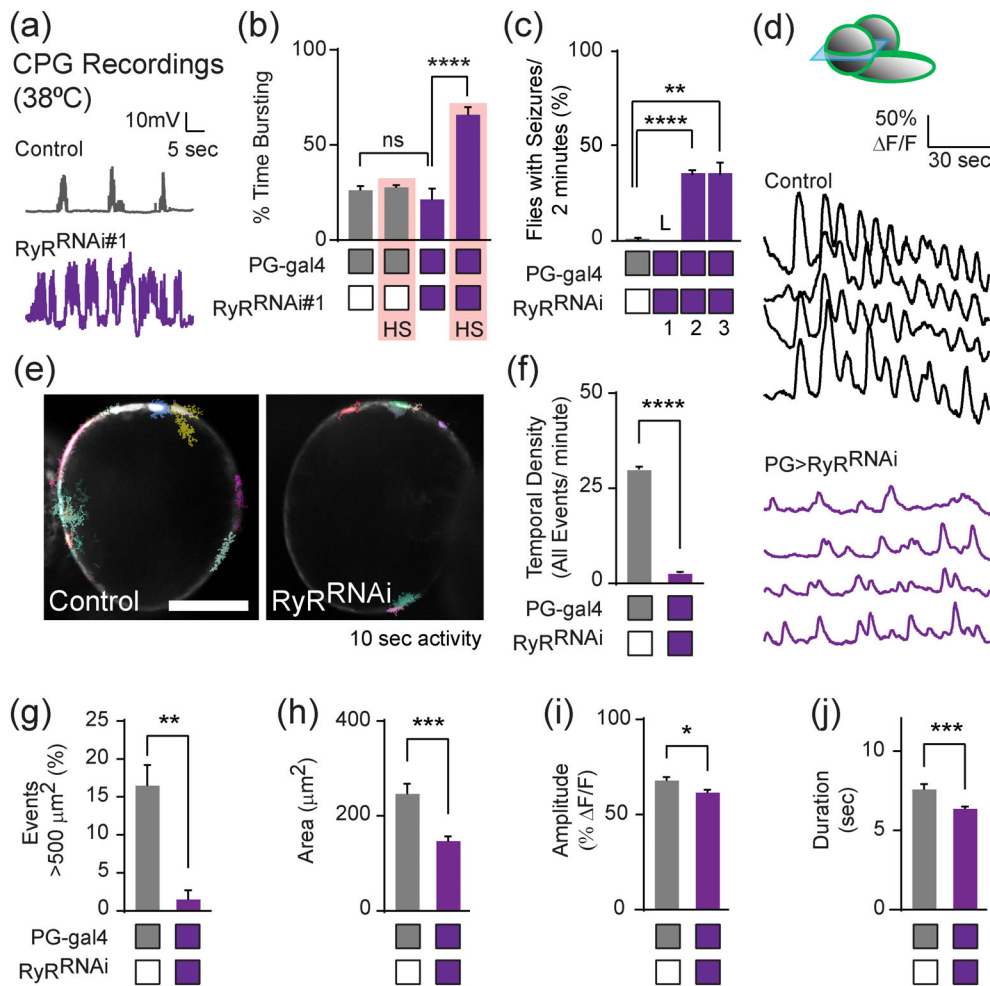


**FIGURE 8** RyR mediated Perineurial  $\text{Ca}^{2+}$  wave propagation is crucial for the prevention of seizures. (a, b) CPG activity in PG >  $\text{RyR}^{\text{RNAi}}$ . (a) Representative voltage traces of spontaneous CPG activity recorded at larval 3<sup>rd</sup> instar muscle 6 at 38°C in control and PG >  $\text{RyR}^{\text{RNAi}}$  animals ( $n \geq 5$  preparations/genotype). (b) Quantification of percent time bursting for CPG recordings of PG >  $\text{RyR}^{\text{RNAi}}$  animals at room temperature and after a 38°C heat-shock (HS, marked with pink shading) ( $p < 0.0001$ , One-way ANOVA,  $n \geq 5$  preparations/genotype). (c) Histogram summarizing the percent of flies exhibiting heat-shock induced seizures at 2 min (38.5°C) following PG knockdown of RyR with 3 non-overlapping RNAi hairpins (L = adult lethal for RNAi#1,  $p < 0.0001$  for RNAi#2,  $p < 0.01$  for RNAi#3, One-way ANOVA,  $N = 4$  groups of >10 flies/genotype). (d–j) Imaging of PG >  $\text{myr}::\text{GCaMP6s}$  in dissected 3<sup>rd</sup> instar PG >  $\text{RyR}^{\text{RNAi}\#1}$  *Drosophila* larvae. (d) *Top*, schematic representation of the *Drosophila* larval brain shows the relative field of view at the dorsal surface of the VNC (light blue). *Bottom*, representative traces of mean (%  $\Delta\text{F}/\text{F}$ ) show that PG  $\text{Ca}^{2+}$  activity is decreased in PG >  $\text{RyR}^{\text{RNAi}\#1}$  animals compared to controls. (e) 10 s activity projection showing the total temporal density of  $\text{Ca}^{2+}$  elevations in control and PG >  $\text{RyR}^{\text{RNAi}}$  animals. Scale bar, 100  $\mu\text{m}$ . (f–j) Comparisons of  $\text{Ca}^{2+}$  transient characteristics in brain-PG of control and PG >  $\text{RyR}^{\text{RNAi}}$  animals. Data was derived from event-based detection (AQuA, see methods).  $N = 5$  animals/4 min imaging session each/genotype. Brain-PG activity in  $\text{RyR}^{\text{RNAi}}$  animals show significant decreases in the total temporal density of  $\text{Ca}^{2+}$  events (f,  $p < 0.0001$ , Student's *t* test) and wide-spread event occurrence (g,  $>400 \mu\text{m}^2$ ,  $p < 0.01$ , Student's *t* test). The remaining  $\text{Ca}^{2+}$  activity in  $\text{RyR}^{\text{RNAi}}$  animals show significantly smaller area (h,  $p < 0.001$ , Student's *t* test), smaller amplitudes (i,  $p < 0.01$ , Student's *t* test), and shorter event durations (j,  $p < 0.001$ , Student's *t* test). \* =  $p < 0.05$ , \*\* =  $p < 0.01$ , \*\*\* =  $p < 0.001$ , \*\*\*\* =  $p < 0.0001$

controlling neuronal excitability, as knockdown of SOCE components or manipulation of gap junction function impairs basal motor activity and increases seizure susceptibility. These data indicate PG  $\text{Ca}^{2+}$  signaling involves store-dependent  $\text{Ca}^{2+}$  signaling and is essential for maintaining normal nervous system function.

A key question moving forward is how PG  $\text{Ca}^{2+}$  waves mechanistically regulate brain function. Maintenance of neuronal excitability requires a fine-tuned extracellular ion balance and a steady supply of nutrients and metabolites. This homeostasis is achieved by

evolutionary conserved specialized structures that form the blood-brain barrier (BBB). The primary function of the BBB is to maintain homeostasis by regulating influx and efflux transport, a role that requires tight cell-to-cell interactions. The mammalian BBB consists of endothelial cells, astrocytes, pericytes, neurons, and microglia which shape the homeostatic function of the barrier (Alvarez, Katayama, & Prat, 2013). Several components of the BBB, including endothelial cells, astrocytes and pericytes exhibit fluctuations in intracellular  $\text{Ca}^{2+}$ , suggesting a generalized role for  $\text{Ca}^{2+}$  activity in BBB function

(Fujii, Maekawa, & Morita, 2017; Nagashima et al., 1997; Paemeleire, de Hemptinne, & Leybaert, 1999; Scemes & Giaume, 2006). In *Drosophila*, the BBB is formed by two glial layers: the PG and SPG cells (Figure 1(a)). The main barrier function is attributed to SPG cells that form pleated septate junctions and prevent paracellular diffusion, similar to tight junctions in the mammalian endothelial BBB. PG establish the first diffusion barrier, perform structural roles (i.e. secretion of the neural lamella and providing rigidity to the CNS) and provide SPG with metabolic support, although their exact contribution to BBB function is not fully understood (Limmer, Weiler, Volkenhoff, Babatz, & Klambt, 2014; Schirmeier & Klambt, 2015; Stork, et al., 2008; Yildirim, et al., 2019). We did not find defects in the gross morphology of PG when PG  $\text{Ca}^{2+}$  waves were disrupted. Similarly, the BBB diffusion barrier as assayed with dextran dye penetration was unaffected. As such, PG  $\text{Ca}^{2+}$  waves are likely to regulate either small molecule diffusion, SPG cell function or secretion of unknown factors from PG cells to shape neuronal excitability.

While interference with SOCE and the spread of  $\text{Ca}^{2+}$  waves across the PG sheet alters behavior and increases seizure susceptibility, the mechanism(s) downstream of intracellular  $\text{Ca}^{2+}$  changes that alter neuronal excitability is unknown. Based on our current observations, the different signatures in PG  $\text{Ca}^{2+}$  signaling across different brain regions suggest that although all PG cells utilize ER-store-dependent  $\text{Ca}^{2+}$  signaling, distinct PG cell populations may employ intracellular  $\text{Ca}^{2+}$  signaling in unique ways. The *Drosophila* hemolymph-brain barrier (PG and SPG) expresses numerous transporters and receptors that selectively move nutrients, metabolites and other compounds in and out of the brain (DeSalvo, et al., 2014). Hence, one possible mechanism by which PG  $\text{Ca}^{2+}$  could alter neuronal activity is through regulation of transport across the BBB. First, PG  $\text{Ca}^{2+}$  activity could modulate exocytotic/endocytotic cycling of membrane proteins within the PG layer itself, similar to its role in regulating surface levels of  $\text{K}^+$  channels in cortex glia (Weiss, et al., 2019) and GABA transporters in astrocyte-like glia (Zhang, et al., 2017). Second, PG  $\text{Ca}^{2+}$  may regulate transport in SPG cells via a cell non-autonomous mechanism. A recent study found that efflux transporters in *Drosophila* SPG cells were regulated by a circadian clock in PG cells (Zhang, Yue, Arnold, Artiushin, & Sehgal, 2018). In this study, changes in PG  $\text{Mg}^{2+}$  balance were shown to regulate the activity levels of Pgp transporters (belong to the ATP-binding cassette [ABC] transporter family) in SPG cells (Zhang, et al., 2018). Though the gross anatomy of the BBB and basic diffusion of large molecules across the barrier were not affected, regulation of more subtle aspects of BBB transport of small molecules such as ions and metabolites could be altered. PG cells also play structural roles by secreting proteins composing the neural lamella and providing rigidity to the CNS (Yildirim, et al., 2019). As such, impairments in the fine structure of the BBB might indirectly affect transport. At the *Drosophila* neuromuscular junction (NMJ),  $\text{Ca}^{2+}$  release from the ER is involved in microtubule stabilization (Wong et al., 2014), and disruption in this process impairs synaptic growth, synaptic vesicle release probability and decrease synaptic transmission. Thus, loss of PG SOCE and subsequent depletion of ER  $\text{Ca}^{2+}$  stores might directly influence the secretion of proteins that compose the neural lamina, or

induce destabilization of PG microtubules and alter rigidity that is crucial for brain homeostasis and function (Yildirim, et al., 2019). Further studies will be required to define how PG  $\text{Ca}^{2+}$  waves ultimately control neuronal excitability and whether different PG populations use distinct intracellular  $\text{Ca}^{2+}$  signaling pathways that are dependent on their unique  $\text{Ca}^{2+}$  wave dynamics.

Single-cell transcriptomic analyses of mammalian glial subtypes, including astrocytes, have advanced our understanding of astrocyte diversity. Astrocytes from different brain regions, as well as within the same region, have distinct transcriptomic profiles that allow classification into novel subpopulations with unique spatial distribution and signaling pathways (Khakh & Deneen, 2019; Yu, Nagai, & Khakh, 2020). To date, no molecular differences have been described between PG cells derived from the CNS or PNS, and despite morphological differences, PG cells are thought to share similar functional properties (Yildirim, et al., 2019). Transcriptomic analysis of *Drosophila* surface glia (PG and SPG together) demonstrated these cells collectively show molecular signatures similar to vertebrate brain-vascular endothelial cells that form the BBB (DeSalvo, et al., 2014). However, this analysis lacked single-cell resolution required for a molecular distinction of PG cells from different brain areas. Single-cell transcriptomic analysis of the *Drosophila* brain displayed relatively low coverage of PG cells (~70 cells, [Davie et al., 2018]), preventing any distinction between possible subpopulations. Our data suggest PG cells derived from different brain regions can be distinguished based on  $\text{Ca}^{2+}$  wave dynamics, and further transcriptomic analyses might yield insights into the diversity of PG cells and glial cells in general.

Although astrocytes were traditionally considered to serve only supportive functions in the brain, the discovery of astrocytic intracellular  $\text{Ca}^{2+}$  signals has changed our view of how these cells contribute to brain function. Accumulating data indicate astrocytes can respond to neuronal activity and regulate neuronal function via intracellular astrocytic  $\text{Ca}^{2+}$  signaling. However, the functional consequences of glial  $\text{Ca}^{2+}$  signaling on neuronal physiology and brain function are not fully understood. One of the controversies in the field of glial biology is the functional distinction between ER-mediated somatic  $\text{Ca}^{2+}$  oscillations and near-membrane microdomain  $\text{Ca}^{2+}$  oscillations in glial processes. A central mechanism in intracellular  $\text{Ca}^{2+}$  signaling is the SOCE pathway which re-fills ER  $\text{Ca}^{2+}$  stores upon depletion triggered by a signaling cascade. In this pathway, the gating of the plasma membrane  $\text{Ca}^{2+}$  channel, Orai, is controlled by the ER-localized  $\text{Ca}^{2+}$  sensor, Stim, leading to  $\text{Ca}^{2+}$  influx and restoration of the ER  $\text{Ca}^{2+}$  store. While Orai and Stim expression have been detected in mammalian astroglia, the role of SOCE in glial biology is yet to be fully characterized. Our functional analysis indicates SOCE is a critical  $\text{Ca}^{2+}$  signaling pathway in PG cells that can act independently of  $\text{IP}_3$  receptors.

Accumulating evidence indicate glia are likely to play a central role in a host of neurological disorders, with multiple disease-associated genes enriched in glial subtypes (Kelley, Nakao-Inoue, Molofsky, & Oldham, 2018). Studies investigating the mechanisms underlying epileptic seizures have primarily focused on neuronal origins, though accumulating evidence highlights an important role of non-neuronal cells in both the generation and spread of epileptic



seizures in the brain. In this study, we found that alterations in the SOCE pathway in the *Drosophila* BBB lead to seizure-like episodes without affecting basic barrier function. This suggests that SOCE within the BBB regulates more subtle processes such as the regulation of active transport of small molecules or ions. In vertebrates, a tight connection between seizures and BBB dysfunction has also been found, with some studies showing that prolonged seizures or brain injury can lead to changes in BBB properties and subsequent BBB dysfunction, and other studies suggesting a causative role for BBB dysfunction in epileptogenesis (Gorter, Aronica, & van Vliet, 2019; van Vliet, Aronica, & Gorter, 2015). Future characterization of how glial Ca<sup>2+</sup> signaling within the *Drosophila* BBB actively shapes neuronal excitability should shed light on the broader role of BBB function in the generation of seizures and suggest potential new treatment targets for epilepsy.

## ACKNOWLEDGMENTS

This work was supported by NIH grants NS40296 and MH104536 to JTL, Israel Science Foundation (ISF) grant 343/18 and the German Research Foundation (DFG) grant 408264519 to MP, the Shamir Fellowship from the Israeli Ministry for Science and Technology and the Teva's Bio-Innovation Fellowship to SW. We thank the Bloomington *Drosophila* Stock Center (NIHP40OD018537), the Vienna *Drosophila* RNAi Center, the Harvard TriP Project, Vanessa Auld (University of British Columbia), Andrea Brand (Gurdon Institute) for providing *Drosophila* strains, Mikoshiba Hiroko for providing OER: GCaMP6f contract, and members of the Littleton and Parnas labs for helpful discussions and comments on the manuscript.

## CONFLICT OF INTEREST

The authors declare no potential conflict of interest.

## AUTHOR CONTRIBUTION

Shirley Weiss, Conceptualization, Data curation, Formal analysis, Investigation, Writing—original draft, review and editing; Lauren C Clamon, Julia E Manoim and Kiel G Ormerod, Data curation; Moshe Parnas and J Troy Littleton, Conceptualization, Supervision, Writing—original draft, review and editing

## DATA AVAILABILITY STATEMENT

Data Availability Statement: The data that support the findings of this study are available from the corresponding author upon request.

## ORCID

Shirley Weiss  <https://orcid.org/0000-0002-1006-349X>

## REFERENCES

- Abbott, N. J., Ronnback, L., & Hansson, E. (2006). Astrocyte-endothelial interactions at the blood-brain barrier. *Nature Reviews Neuroscience*, 7(1), 41–53. <https://doi.org/10.1038/nrn1824>
- Agarwal, A., Wu, P.-H., Hughes, E. G., Fukaya, M., Tischfield, M. A., Langseth, A. J., Wirtz, D., & Bergles, D. E. (2017). Transient opening of the mitochondrial permeability transition pore induces microdomain calcium transients in astrocyte processes. *Neuron*, 93(3), 587–605. <https://doi.org/10.1016/j.neuron.2016.12.034>
- Alvarez, J. I., Katayama, T., & Prat, A. (2013). Glial influence on the blood brain barrier. *Glia*, 61(12), 1939–1958. <https://doi.org/10.1002/glia.22575>
- Barres, B. A. (2008). The mystery and magic of glia: A perspective on their roles in health and disease. *Neuron*, 60(3), 430–440. <https://doi.org/10.1016/j.neuron.2008.10.013>
- Bazargani, N., & Attwell, D. (2016). Astrocyte calcium signaling: The third wave. *Nature Neuroscience*, 19(2), 182–189. <https://doi.org/10.1038/nn.4201>
- Bielopolski, N., Amin, H., Apostolopoulou, A. A., Rozenfeld, E., Lerner, H., Huetteroth, W., Lin, A. C., & Parnas, M. (2019). Inhibitory muscarinic acetylcholine receptors enhance aversive olfactory learning in adult drosophila. *Elife*, 8, e48264. <https://doi.org/10.7554/eLife.48264>
- Bindocci, E., Savtchouk, I., Liaudet, N., Becker, D., Carriero, G., & Volterra, A. (2017). Three-dimensional Ca<sup>2+</sup> imaging advances understanding of astrocyte biology. *Science*, 356(6339), eaai8185.
- Burdyga, T., & Borysova, L. (2018). Ca<sup>2+</sup> Signalling in Pericytes. *Advances in Experimental Medicine and Biology*, 1109, 95–109. [https://link.springer.com/chapter/10.1007%2F978-3-030-02601-1\\_8](https://link.springer.com/chapter/10.1007%2F978-3-030-02601-1_8)
- Chai, H., Diaz-Castro, B., Shigetomi, E., Monte, E., Octeau, J. C., Yu, X., Cohn, W., Rajendran, P. S., Vondriska, T. M., Whitelegge, J. P., Coppola, G., & Khakh, B. S. (2017). Neural circuit-specialized astrocytes: Transcriptomic, proteomic, morphological, and functional evidence. *Neuron*, 95(3), 531–549.
- Chen, T. W., Wardill, T. J., Sun, Y., Pulver, S. R., Renninger, S. L., Baohan, A., Schreiter, E. R., Kerr, R. A., Orger, M. B., Jayaraman, V., Looger, L. L., Svoboda, K., & Kim, D. S. (2013). Ultrasensitive fluorescent proteins for imaging neuronal activity. *Nature*, 499(7458), 295–300.
- Claridge-Chang, A., Roorda, R. D., Vrontou, E., Sjulson, L., Li, H., Hirsh, J., & Miesenböck, G. (2009). Writing memories with light-addressable reinforcement circuitry. *Cell*, 139(2), 405–415.
- Clarke, B. E., Taha, D. M., Tyzack, G. E., & Patani, R. (2021). Regionally encoded functional heterogeneity of astrocytes in health and disease: a perspective. *Glia*, 69(1), 20–27. <https://doi.org/10.1002/glia.23877>
- Davie, K., Janssens, J., Koldere, D., De Waegeneer, M., Pech, U., Kreft, L., ... Aerts, S. (2018). A single-cell transcriptome atlas of the aging drosophila brain. *Cell*, 174(4), 982–998.
- Dawydow, A., Gueta, R., Ljaschenko, D., Ullrich, S., Hermann, M., Ehmann, N., Gao, S., Fiala, A., Langenhan, T., Nagel, G., & Kittel, R. J. (2014). Channelrhodopsin-2-XXL, a powerful optogenetic tool for low-light applications. *Proceedings of the National Academy of Sciences*, 111(38), 13972–13977. <https://doi.org/10.1073/pnas.1408269111>
- Deb, B. K., Pathak, T., & Hasan, G. (2016). Store-independent modulation of Ca<sup>2+</sup> entry through Orai by Septin 7. *Nature Communications*, 7, 11751.
- DeSalvo, M. K., Hindle, S. J., Rusan, Z. M., Orng, S., Eddison, M., Halliwill, K., & Bainton, R. J. (2014). The drosophila surface glia transcriptome: Evolutionary conserved blood-brain barrier processes. *Frontiers in Neuroscience*, 8, 346.
- DeSalvo, M. K., Mayer, N., Mayer, F., & Bainton, R. J. (2011). Physiologic and anatomic characterization of the brain surface glia barrier of drosophila. *Glia*, 59(9), 1322–1340.
- Di Castro, M. A., Chuquet, J., Liaudet, N., Bhaukaurally, K., Santello, M., Bouvier, D., Pascale, T., & Volterra, A. (2011). Local Ca<sup>2+</sup> detection and modulation of synaptic release by astrocytes. *Nature Neuroscience*, 14(10), 1276–1284. <https://doi.org/10.1038/nn.2929>
- Duffy, J. B. (2002). GAL4 system in drosophila: A fly geneticist's Swiss army knife. *Genesis*, 34(1-2), 1–15. <https://doi.org/10.1002/gene.10150>
- Dunn, K. M., Hill-Eubanks, D. C., Liedtke, W. B., & Nelson, M. T. (2013). TRPV4 channels stimulate Ca<sup>2+</sup>-induced Ca<sup>2+</sup> release in astrocytic endfeet and amplify neurovascular coupling responses. *Proceedings of the National Academy of Sciences*, 110(15), 6157–6162. <https://doi.org/10.1073/pnas.1216514110>

- Fujii, Y., Maekawa, S., & Morita, M. (2017). Astrocyte calcium waves propagate proximally by gap junction and distally by extracellular diffusion of ATP released from volume-regulated anion channels. *Scientific Reports*, 7(1), 13115.
- Giordano, F., Saheki, Y., Idevall-Hagren, O., Colombo, S. F., Pirruccello, M., Milosevic, I., Gracheva, E. O., Bagriantsev, S. N., Borgese, N., & De Camilli, P. (2013). PI(4,5)P(2)-dependent and  $Ca^{2+}$ -regulated ER-PM interactions mediated by the extended synaptotagmins. *Cell*, 153(7), 1494–1509. <https://doi.org/10.1016/j.cell.2013.05.026>
- Gorter, J. A., Aronica, E., & Van Vliet, E. A. (2019). The roof is leaking and a storm is raging: Repairing the blood-brain barrier in the fight against epilepsy. *Epilepsy Currents*, 19(3), 177–181.
- Green, E. W., O'Callaghan, E. K., Pegoraro, M., Armstrong, J. D., Costa, R., & Kyriacou, C. P. (2015). Genetic analysis of drosophila circadian behavior in seminatural conditions. *Methods Enzymol*, 551, 121–133. <https://doi.org/10.1016/bs.mie.2014.10.001>
- Haustein, M. D., Kracun, S., Lu, X. H., Shih, T., Jackson-Weaver, O., Tong, X., Xu, J., Yang, X. W., O'Dell, T. J., Marvin, J. S., Ellisman, M. H., Bushong, E. A., Looger, L. L., & Khakh, B. S. (2014). Conditions and constraints for astrocyte calcium signaling in the hippocampal mossy fiber pathway. *Neuron*, 82(2), 413–429. <https://doi.org/10.1016/j.neuron.2014.02.041>
- Hayashi, S., Ito, K., Sado, Y., Taniguchi, M., Akimoto, A., Takeuchi, H., Aigaki, T., Matsuzaki, F., Nakagoshi, H., Tanimura, T., Ueda, R., Uemura, T., Yoshihara, M., & Goto, S. (2002). GETDB, a database compiling expression patterns and molecular locations of a collection of Gal4 enhancer traps. *Genesis*, 34(1–2), 58–61. <https://doi.org/10.1002/gene.10137>
- Holcroft, C. E., Jackson, W. D., Lin, W. H., Bassiri, K., Baines, R. A., & Phelan, P. (2013). Innexins *Ogre* and *Inx2* are required in glial cells for normal postembryonic development of the drosophila central nervous system. *Journal of Cell Science*, 126(Pt 17), 3823–3834. <https://doi.org/10.1242/jcs.117994>
- Hua, X., Malarkey, E. B., Sunjara, V., Rosenwald, S. E., Li, W. H., & Parpura, V. (2004).  $Ca^{2+}$ -dependent glutamate release involves two classes of endoplasmic reticulum  $Ca^{2+}$  stores in astrocytes. *Journal of Neuroscience Research*, 76(1), 86–97. <https://doi.org/10.1002/jnr.20061>
- Jiang, R., Diaz-Castro, B., Looger, L. L., & Khakh, B. S. (2016). Dysfunctional calcium and glutamate signaling in striatal astrocytes from Huntington's disease model mice. *Journal of Neuroscience*, 36(12), 3453–3470. <https://doi.org/10.1523/jneurosci.3693-15.2016>
- Kanamaru, K., Sekiya, H., Xu, M., Satoh, K., Kitajima, N., Yoshida, K., Okubo, Y., Sasaki, T., Moritoh, S., Hasuwa, H., Mimura, M., Horikawa, K., Matsui, K., Nagai, T., Iino, M., & Tanaka, K. F. (2014). In vivo visualization of subtle, transient, and local activity of astrocytes using an ultrasensitive  $Ca^{2+}$  indicator. *Cell Reports*, 8(1), 311–318. <https://doi.org/10.1016/j.celrep.2014.05.056>
- Kelley, K. W., Nakao-Inoue, H., Molofsky, A. V., & Oldham, M. C. (2018). Variation among intact tissue samples reveals the core transcriptional features of human CNS cell classes. *Nature Neuroscience*, 21(9), 1171–1184. <https://doi.org/10.1038/s41593-018-0216-z>
- Khakh, B. S., & Deneen, B. (2019). The emerging nature of astrocyte diversity. *Annual Review of Neuroscience*, 42, 187–207. <https://doi.org/10.1146/annurev-neuro-070918-050443>
- Khakh, B. S., & McCarthy, K. D. (2015). Astrocyte calcium signaling: From observations to functions and the challenges therein. *Cold Spring Harbor Perspectives Biology*, 7(4), a020404.
- Kikuma, K., Li, X., Kim, D., Sutter, D., & Dickman, D. K. (2017). Extended Synaptotagmin localizes to presynaptic ER and promotes neurotransmission and synaptic growth in drosophila. *Genetics*, 207(3), 993–1006. <https://doi.org/10.1534/genetics.117.300261>
- Kohn, E., Katz, B., Yasin, B., Peters, M., Rhodes, E., Zaguri, R., Weiss S., & Minke, B. (2015). Functional cooperation between the IP3 receptor and phospholipase C secures the high sensitivity to light of Drosophila photoreceptors in vivo. *Journal of Neuroscience*, 35(6), 2530–2546. <https://doi.org/10.1523/jneurosci.3933-14.2015>
- Kremer, M. C., Jung, C., Batelli, S., Rubin, G. M., & Gaul, U. (2017). The glia of the adult drosophila nervous system. *Glia*, 65(4), 606–638. <https://doi.org/10.1002/glia.23115>
- Lee, B. P., & Jones, B. W. (2005). Transcriptional regulation of the drosophila glial gene repo. *Mechanisms of Development*, 122(6), 849–862. <https://doi.org/10.1016/j.mod.2005.01.002>
- Limmer, S., Weiler, A., Volkenhoff, A., Babatz, F., & Klambt, C. (2014). The drosophila blood-brain barrier: Development and function of a glial endothelium. *Frontiers in Neuroscience*, 8, 365.
- Livak, K. J., & Schmittgen, T. D. (2001). Analysis of relative gene expression data using real-time quantitative PCR and the  $2^{-\Delta\Delta CT}$  method. *Methods*, 25(4), 402–408. <https://doi.org/10.1006/meth.2001.1262>
- Ma, Z., Stork, T., Bergles, D. E., & Freeman, M. R. (2016). Neuromodulators signal through astrocytes to alter neural circuit activity and behaviour. *Nature*, 539(7629), 428–432. <https://doi.org/10.1038/nature20145>
- Matyash, M., Matyash, V., Nolte, C., Sorrentino, V., & Kettenmann, H. (2002). Requirement of functional ryanodine receptor type 3 for astrocyte migration. *The FASEB Journal*, 16(1), 84–86. <https://doi.org/10.1096/fj.01-0380fje>
- Melom, J. E., & Littleton, J. T. (2013). Mutation of a NCKX eliminates glial microdomain calcium oscillations and enhances seizure susceptibility. *Journal of Neuroscience*, 33(3), 1169–1178. <https://doi.org/10.1523/jneurosci.3920-12.2013>
- Nagai, J., Yu, X., Papouin, T., Cheong, E., Freeman, M. R., Monk, K. R., Hastings, M. H., Haydon, P. G., Rowitch, D., Shaham, S., & Khakh, B. S. (2021). Behaviorally consequential astrocytic regulation of neural circuits. *Neuron*, 109(4), 576–596. <https://doi.org/10.1016/j.neuron.2020.12.008>
- Nagashima, T., Ikeda, K., Wu, S., Kondo, T., Yamaguchi, M., & Tamaki, N. (1997). The mechanism of reversible osmotic opening of the blood-brain barrier: Role of intracellular calcium ion in capillary endothelial cells. *Acta Neurochirurgica Supplement*, 70, 231–233. [https://doi.org/10.1007/978-3-7091-6837-0\\_1](https://doi.org/10.1007/978-3-7091-6837-0_1)
- Niwa, F., Sakuragi, S., Kobayashi, A., Takagi, S., Oda, Y., Bannai, H., & Mikoshiba, K. (2016). Dissection of local  $Ca^{2+}$  signals inside cytosol by ER-targeted  $Ca^{2+}$  indicator. *Biochemical and Biophysical Research Communications*, 479(1), 67–73. <https://doi.org/10.1016/j.bbrc.2016.09.034>
- Otsu, Y., Couchman, K., Lyons, D. G., Collot, M., Agarwal, A., Mallet, J. M., Pfrieger, F. W., Bergles, D. E., & Charpak, S. (2015). Calcium dynamics in astrocyte processes during neurovascular coupling. *Nature Neuroscience*, 18(2), 210–218. <https://doi.org/10.1038/nn.3906>
- Paemeleire, K., de Hemptinne, A., & Leybaert, L. (1999). Chemically, mechanically, and hyperosmolarity-induced calcium responses of rat cortical capillary endothelial cells in culture. *Experimental Brain Research*, 126(4), 473–481. <https://doi.org/10.1007/s002210050755>
- Panatier, A., Vallee, J., Haber, M., Murai, K. K., Lacaillie, J. C., & Robitaille, R. (2011). Astrocytes are endogenous regulators of basal transmission at central synapses. *Cell*, 146(5), 785–798. <https://doi.org/10.1016/j.cell.2011.07.022>
- Parnas, M., Lin, A. C., Huetteroth, W., & Miesenbock, G. (2013). Odor discrimination in Drosophila: from neural population codes to behavior. *Neuron*, 79(5), 932–944. <https://doi.org/10.1016/j.neuron.2013.08.006>
- Petersen, C. E., Wolf, M. J., & Smyth, J. T. (2020). Suppression of store-operated calcium entry causes dilated cardiomyopathy of the Drosophila heart. *Biology Open*, <https://doi.org/10.1242/bio.049999>
- Rodriguez-Prados, M., Rojo-Ruiz, J., Garcia-Sancho, J., & Alonso, M. T. (2020). Direct monitoring of ER  $Ca^{2+}$  dynamics reveals that  $Ca^{2+}$  entry induces ER- $Ca^{2+}$  release in astrocytes. *Pflügers Archiv - European Journal of Physiology*, 472(4), 439–448. <https://doi.org/10.1007/s00424-020-02364-7>
- Rozenfeld, E., Lerner, H., & Parnas, M. (2019). Muscarinic modulation of antennal lobe GABAergic local neurons shapes odor coding and behavior. *Cell Reports*, 29(10), 3253–3265.



- Rungta, R. L., Bernier, L. P., Dissing-Olesen, L., Groten, C. J., LeDue, J. M., Ko, R., Drissler, S., & MacVicar, B. A. (2016). Ca<sup>2+</sup> transients in astrocyte fine processes occur via Ca<sup>2+</sup> influx in the adult mouse hippocampus. *Glia*, 64(12), 2093–2103.
- Scemes, E., & Giaume, C. (2006). Astrocyte calcium waves: what they are and what they do. *Glia*, 54(7), 716–725. <https://doi.org/10.1002/glia.20374>
- Schirmeier, S., & Klambt, C. (2015). The Drosophila blood-brain barrier as interface between neurons and hemolymph. *Mechanisms of Development*, 138(Pt 1), 50–55. <https://doi.org/10.1016/j.mod.2015.06.002>
- Shigetomi, E., Bowser, D. N., Sofroniew, M. V., & Khakh, B. S. (2008). Two forms of astrocyte calcium excitability have distinct effects on NMDA receptor-mediated slow inward currents in pyramidal neurons. *Journal of Neuroscience*, 28(26), 6659–6663. <https://doi.org/10.1523/jneurosci.1717-08.2008>
- Shigetomi, E., Bushong, E. A., Hausteiner, M. D., Tong, X., Jackson-Weaver, O., Kracun, S., Xu, J., Sofroniew, M. V., Ellisman, M. H., & Khakh, B. S. (2013). Imaging calcium microdomains within entire astrocyte territories and endfeet with GCaMPs expressed using adeno-associated viruses. *Journal of General Physiology*, 141(5), 633–647. <https://doi.org/10.1085/jgp.201210949>
- Shigetomi, E., Kracun, S., Sofroniew, M. V., & Khakh, B. S. (2010). A genetically targeted optical sensor to monitor calcium signals in astrocyte processes. *Nature Neuroscience*, 13(6), 759–766. <https://doi.org/10.1038/nn.2557>
- Shigetomi, E., Tong, X., Kwan, K. Y., Corey, D. P., & Khakh, B. S. (2012). TRPA1 channels regulate astrocyte resting calcium and inhibitory synapse efficacy through GAT-3. *Nature Neuroscience*, 15(1), 70–80. <https://doi.org/10.1038/nn.3000>
- Speder, P., & Brand, A. H. (2014). Gap junction proteins in the blood-brain barrier control nutrient-dependent reactivation of drosophila neural stem cells. *Developmental Cell*, 30(3), 309–321. <https://doi.org/10.1016/j.devcel.2014.05.021>
- Srinivasan, R., Huang, B. S., Venugopal, S., Johnston, A. D., Chai, H., Zeng, H., Golshani, P., & Khakh, B. S. (2015). Ca<sup>2+</sup> signaling in astrocytes from *lpr2(-/-)* mice in brain slices and during startle responses in vivo. *Nature Neuroscience*, 18(5), 708–717. <https://doi.org/10.1038/nn.4001>
- Stobart, J. L., Ferrari, K. D., Barrett, M. J. P., Stobart, M. J., Looser, Z. J., Saab, A. S., & Weber, B. (2018). Long-term in vivo calcium imaging of astrocytes reveals distinct cellular compartment responses to sensory stimulation. *Cerebral Cortex*, 28(1), 184–198. <https://doi.org/10.1093/cercor/bhw366>
- Stork, T., Engelen, D., Krudewig, A., Silies, M., Bainton, R. J., & Klambt, C. (2008). Organization and function of the blood-brain barrier in Drosophila. *Journal of Neuroscience*, 28(3), 587–597. <https://doi.org/10.1523/jneurosci.4367-07.2008>
- Straub, S. V., Bonev, A. D., Wilkerson, M. K., & Nelson, M. T. (2006). Dynamic inositol trisphosphate-mediated calcium signals within astrocytic endfeet underlie vasodilation of cerebral arterioles. *The Journal of General Physiology*, 128(6), 659–669. <https://doi.org/10.1085/jgp.200609650>
- van Vliet, E. A., Aronica, E., & Gorter, J. A. (2015). Blood-brain barrier dysfunction, seizures and epilepsy. *Seminars in Cell and Developmental Biology*, 38, 26–34. <https://doi.org/10.1016/j.semcdb.2014.10.003>
- Wang, Y., DelRosso, N. V., Vaidyanathan, T. V., Cahill, M. K., Reitman, M. E., Pittolo, S., Mi, X., Yu, G., & Poskanzer, K. E. (2019). Accurate quantification of astrocyte and neurotransmitter fluorescence dynamics for single-cell and population-level physiology. *Nature Neuroscience*, 22(11), 1936–1944. <https://doi.org/10.1038/s41593-019-0492-2>
- Weiss, S., Melom, J. E., Ormerod, K. G., Zhang, Y. V., & Littleton, J. T. (2019). Glial ca<sup>2+</sup> signaling links endocytosis to K<sup>(+)</sup> buffering around neuronal somas to regulate excitability. *Elife*, 8, e44186. <https://doi.org/10.7554/eLife.44186>
- Wong, C. O., Chen, K., Lin, Y. Q., Chao, Y., Duraine, L., Lu, Z., Yoon, W. H., Sullivan, J. M., Broadhead, G. T., Sumner, C. J., Lloyd, T. E., Macleod, G. T., Bellen, H. J., & Venkatachalam, K. (2014). A TRPV channel in drosophila motor neurons regulates presynaptic resting Ca<sup>2+</sup> levels, synapse growth, and synaptic transmission. *Neuron*, 84(4), 764–777. <https://doi.org/10.1016/j.neuron.2014.09.030>
- Xie, X., & Auld, V. J. (2011). Integrins are necessary for the development and maintenance of the glial layers in the drosophila peripheral nerve. *Development*, 138(17), 3813–3822. <https://doi.org/10.1242/dev.064816>
- Yang, C. H., Rumpf, S., Xiang, Y., Gordon, M. D., Song, W., Jan, L. Y., & Jan, Y. N. (2009). Control of the postmating behavioral switch in drosophila females by internal sensory neurons. *Neuron*, 61(4), 519–526. <https://doi.org/10.1016/j.neuron.2008.12.021>
- Yildirim, K., Petri, J., Kottmeier, R., & Klambt, C. (2019). Drosophila glia: Few cell types and many conserved functions. *Glia*, 67(1), 5–26. <https://doi.org/10.1002/glia.23459>
- Yu, X., Nagai, J., & Khakh, B. S. (2020). Improved tools to study astrocytes. *Nature Reviews Neuroscience*, 21(3), 121–138. <https://doi.org/10.1038/s41583-020-0264-8>
- Zhang, S. L., Yue, Z., Arnold, D. M., Artiushin, G., & Sehgal, A. (2018). A circadian clock in the blood-brain barrier regulates xenobiotic efflux. *Cell*, 173(1), 130–139.
- Zhang, Y. V., Ormerod, K. G., & Littleton, J. T. (2017). Astrocyte ca<sup>2+</sup> influx negatively regulates neuronal activity. *eNeuro*, 4(2), ENEURO.0340-ENEU16.2017.

## SUPPORTING INFORMATION

Additional supporting information may be found in the online version of the article at the publisher's website.

**How to cite this article:** Weiss, S., Clamon, L. C., Manoim, J. E., Ormerod, K. G., Parnas, M., & Littleton, J. T. (2022). Glial ER and GAP junction mediated Ca<sup>2+</sup> waves are crucial to maintain normal brain excitability. *Glia*, 70(1), 123–144. <https://doi.org/10.1002/glia.24092>